International Journal of Thermophysics (2026) 47:28
https://doi.org/10.1007/s10765-025-03694-3

Fick Diffusivity, Thermal Diffusivity, Thermal Conductivity, Density, and Mixture Composition of Binary Mixtures of γ-Butyrolactone and 1,4-Butanediol by Light Scattering Techniques and Conventional Methods

Dena Mombeini[1] · Hubert P. Blabus[1] · Michael H. Rausch[1] · Tobias Klein[1] · Thomas M. Koller[1,5] · Chathura J. Kankanamge[1] · Michael Geißelbrecht[2] · Peter Wasserscheid[2,3,4] · Andreas P. Fröba[1]

Received: 5 December 2025 / Accepted: 7 December 2025

Abstract

γ-Butyrolactone (GBL) and 1,4-butanediol (BDO) represent a promising liquid organic hydrogen carrier (LOHC) system, for which a lack of thermophysical property data at process-relevant conditions exists. For this LOHC system, the Fick diffusivity D_{11}, thermal diffusivity a, thermal conductivity λ, and density ρ were investigated at about 0.1 MPa as a function of temperature T and mixture composition at GBL amount fractions $x_{\mathrm{GBL}} = (0.00, 0.25, 0.50, 0.75, \text{and } 1.00)$ using light scattering and conventional techniques. Vibrating U-tube densimetry and a guarded parallel-plate instrument were employed to determine ρ between $T = (283 \text{ and } 473)$ K and λ between $T = (283 \text{ and } 363)$ K. Dynamic light scattering allowed simultaneous access to a and D_{11} between $T = (298 \text{ and } 473)$ K in macroscopic thermodynamic equilibrium, while polarization-difference Raman spectroscopy was applied after calibration to monitor the composition. The onset of a certain decomposition or structural rearrangement was observed above about $T = 398$ K, depending on the sample composition and experimental boundary conditions. When such effects are small, the data for ρ, a, and D_{11} increase with increasing x_{GBL} at a given T, whereas λ has the opposite trend. With the help of the results for ρ, a, and λ, values for the specific isobaric heat capacity c_{p} could be derived. The present measurement results agree with the few experimental data for ρ and λ available in the literature for the pure mixture components and contribute to a significant extension of the thermophysical property database for this highly promising LOHC system.

Keywords γ-butyrolactone · 1,4-butanediol · Thermophysical properties · Liquid organic hydrogen carrier · Dynamic light scattering · Raman spectroscopy

---

Extended author information available on the last page of the article

1 Introduction

The utilization of hydrogen (H_2) as a green carrier for the supply, transport, and storage of energy made available from renewable resources such as wind or solar power is considered to be crucial in the future [1–3]. For this purpose, the implementation of a H_2 economy for safe and cost-efficient energy provision is of high relevance. One critical aspect is related to the safety risks resulting from the high flammability of H_2, which makes its handling complex and requires suitable infrastructures. Another major constraint is the low volumetric energy density of H_2 under ambient temperature and pressure [2]. To increase the energy density, pure H_2 can be stored in the gaseous or liquid state by applying high pressures p up to 70 MPa or low temperatures T down to 20 K [4, 5]. The realization of these conditions, however, includes increased safety risks and high operational costs. An efficient alternative is to store H_2 physically or chemically bound to other substances [6]. In the field of chemical storage of H_2 and its transport, liquid organic hydrogen carrier (LOHC) systems are being extensively investigated [3, 5–11]. Such systems offer several advantages such as the possibility to store H_2 under ambient conditions for long-time periods at prominently high volumetric energy density. In addition, existing infrastructure can be used for the transport and handling of LOHC systems since their chemical and physical properties are similar to those of common hydrocarbon-based chemicals and fossil fuels [2].

In principle, an LOHC system consists of a pair of hydrogen-rich and hydrogen-lean molecules. Such a pair enables storing and releasing of H_2 in repeated catalytic hydrogenation and dehydrogenation reactions in the presence of a solid catalyst material. The exothermic hydrogenation step typically occurs at high H_2 partial pressure, whereas the endothermic dehydrogenation step takes place at lower, often near-atmospheric p [4, 5, 10, 11]. Beneficial criteria for potential LOHC materials include high boiling and low melting points to ensure a liquid state over a broad T range, high hydrogen storage capacity, low toxicity, good technical availability at low cost, low heat demand for the hydrogen release step related to a low reaction enthalpy, and low sample degradation [2]. In the last years, the focus in LOHC research was mainly on hydrocarbon-based aromatic molecules as dehydrogenated substances, e.g., systems based on toluene (TOL), diphenylmethane, benzyltoluene (BT), dibenzyltoluene (DBT), and related mixtures with each other or with comparable substances [5, 10, 12–19]. In addition, LOHC systems containing heteroatoms such as nitrogen or oxygen attracted attention, see, e.g., Refs. [2, 7, 14, 20, 21]. These systems typically require milder T and p conditions for H_2 uptake and release compared to purely hydrocarbon-based LOHCs. In addition, the presence of heteroatoms increases the interactions between the LOHC molecules and the metal-based catalyst material [2], which can be beneficial for reaction kinetics. In the context of oxygen-containing LOHC systems, the pair consisting of γ-butyrolactone (GBL) and its hydrogenated counterpart 1,4-butanediol (BDO) has been suggested as a promising new LOHC system some years ago [1, 22, 23]. Although the gravimetric H_2 storage density of the GBL/BDO pair is only 4.5 wt-% and, thus, lower than for typical hydrocarbon-based LOHC systems with, e.g., 6.1 wt-% for the TOL/methylcyclohexane (MCH) system [5, 23], the GBL/BDO system has an interesting volumetric storage density of 44.9 $kg(H_2)\cdot m^{-3}$ compared to 47.1 $kg(H_2)\cdot m^{-3}$ for the TOL/MCH system. In addition, the GBL/BDO LOHC system offers further advantages. The temperature for the hydrogen release from BDO of about 490 K [23] is approximately 100 K lower than that required for the BT- or DBT-based systems. In addition, the GBL/BDO system exhibits comparatively low reaction enthalpies, which lowers the energy input for the dehydrogenation process significantly. Both GBL and BDO are available in large quantities with an annual production capacity in the range of few million tons [24]. Moreover, both substances are accessible from biomass and offer attractive safety and toxicity profiles [24–26].

To design and optimize LOHC processes and apparatuses, the knowledge of the thermophysical properties of the involved working fluids at process-relevant conditions is of great importance. This necessity is especially pronounced for the transport properties thermal diffusivity a or the related thermal conductivity λ and the Fick diffusivity D_{11} in the case of a binary mixture, which are the key molecular transport coefficients for the characterization of heat and mass transfer. These transport processes have a direct influence on, e.g., the heat management and the kinetics in the reaction processes. In addition, equilibrium properties such as the density ρ and the specific isobaric heat capacity c_p are often required. For pure GBL and BDO as well as their binary mixtures, there is a clear lack of thermophysical property data, even in the absence of H_2. In terms of the aforementioned properties being of interest in the present study, only data related to λ [27, 28], ρ [29–41], and c_p [42, 43] of the pure compounds in the liquid state are available in the literature. While these data are mostly restricted to a limited T range, no data are given for the respective mixtures. As the mixture composition with respect to GBL and BDO changes during the hydrogenation and dehydrogenation cycles, detailed information on the thermophysical properties of the LOHC system as a function of the thermodynamic state variables T, p, and composition is needed. Not only in this respect, access to the current degree of hydrogenation represented by the amount fraction of the hydrogenated compound BDO in the reactor is helpful for process operation.

The present work focuses on the experimental determination of several key thermophysical properties of the potential oxygen-containing LOHC system consisting of GBL, BDO, and their binary mixtures at about 0.1 MPa. For this purpose, different experimental methods were used over a wide T range between (283 and 473) K and amount fractions of GBL of $x_{GBL} = (0.00, 0.25, 0.50, 0.75, \text{and } 1.00)$. A guarded parallel-plate-instrument (GPPI) and the vibrating U-tube method were used to access λ and ρ. Dynamic light scattering (DLS) was employed to determine a and, for the binary mixtures, D_{11}. Polarization-difference Raman spectroscopy (PDRS) was calibrated and used to monitor x_{GBL} and to check the sample stability during the DLS experiments. Based on the measured data for λ, a, and ρ, values for c_p could also be derived. After a detailed introduction of the experimental methods and procedures used, observations regarding the sample stability will be addressed before the final discussion of the obtained thermophysical property data.

Table 1 Specification of the supplier, molar mass M, and purities in terms of mass fraction w or volume fraction ϕ of the used chemicals

component	CAS Number	supplier	M / (g mol^{-1})	specified purity[a]
γ-butyrolactone (GBL)	96–48-0	Thermo Fisher Scientific	86.09	$w = 0.999$
1,4-butanediol (BDO)	110–63-4	Thermo Fisher Scientific	90.12	$w = 0.995$
helium (He)	7440–59-7	Air Liquide Deutschland GmbH	4.0026	$\phi \geq 0.99999$
argon (Ar)	7440–37-1	Air Liquide Deutschland GmbH	39.95	$\phi \geq 0.99999$

[a] Sample purities are given as specified in the certificate of analysis provided by the manufacturers

Table 2 Values from water content measurements of the investigated samples before and after measurements by DLS and GPPI.[a]

x_{GBL}	w_{H2O} / ppm			
	DLS		GPPI	
	before	after	before	after
0.000000	500	3200	490	1426
0.251247	720	2500	698	2559
0.499620	310	5700	301	10,266
0.748977	500	4000	440	10,005
1.000000	300	2400	166	2899

[a] The uncertainty of x_{GBL} is $U(x_{GBL}) = 0.000003$, while the relative uncertainty of the water content is $U_r(w_{H2O}) < 0.2$. All uncertainties are given on a confidence level of 0.95 (coverage factor $k = 2$)

2 Experimental Methods

2.1 Materials and Sample Preparation

Information on the suppliers, molar mass M, and purity of the chemicals used in this work is listed in Table 1. Helium (He) was employed as an inert gas in the sample cell used for DLS measurements. All containers used for sample preparation were initially flushed with argon (Ar) and finally filled with Ar atmosphere to minimize uptake of humidity from ambient air into the hygroscopic LOHC system. The preparation of all binary mixtures of GBL and BDO was carried out gravimetrically using a balance with a precision of 0.1 mg for the mass m with an expanded uncertainty (coverage factor $k = 2$) of $U(m)$ = 1 mg. On this basis, the absolute expanded uncertainty ($k = 2$) of the amount fraction of GBL in the binary mixtures, x_{GBL}, can be specified with $U(x_{GBL}) = 0.000003$ for the mixtures with $x_{GBL} = (0.25, 0.50, \text{and } 0.75)$ used for measurements of ρ, λ, a, and D_{11}. The exact compositions of the mixtures studied regarding λ, a, and D_{11} are listed in Table 2. While the same mixtures with $x_{GBL} = (0.25 \text{ and } 0.75)$ were also used for measuring ρ, an additional mixture with $x_{GBL} = 0.500180$ was studied for this purpose. For the PDRS measurements used to calibrate Raman spectroscopy, a finer composition variation with $x_{\mathrm{GBL}} = (0.10 \text{ to } 0.90)$ in steps of 0.10 was carried out. For this, the exact sample compositions are given in Table S1 of the Supplementary Information.

For the preparation of samples for the measurements of λ with the GPPI, the purchased chemicals were used as received. Prior to the DLS and ρ measurements, nearly all samples were filtered twice using a stack of hydrophilic poly(tetrafluoroethylene) (H-PTFE) syringe filters with pore sizes of (450 and 200) nm to remove particulate impurities. Only the pure GBL used for ρ measurements was not filtered, where it was proven in test measurements that filtering does not have any significant impact on the obtained data. Due to the hygroscopic character of GBL and BDO, the water content of the mixtures in terms of the water mass fraction, w_{H2O}, was determined before and after conducting measurements by DLS and the GPPI using Karl Fischer coulometric titration. The data for w_{H2O} before and after the measurements are also given in Table 2 and have a relative expanded uncertainty ($k = 2$) of less than 0.2. For all samples, the relatively low w_{H2O} values before the experiments below $700 \cdot 10^{-6}$, i.e., below about 700 ppm, increased up to a maximum of about $10{,}000 \cdot 10^{-6}$, i.e., about 10,000 ppm, after the experiments. This increase may be caused by the partially inevitable contact of the samples with surrounding air during the sample processing and/or reactions between the LOHC components during the measurements up to $T = 473$ K, where water could be formed as a side product.

2.2 Vibrating U-tube Method – Density

ρ of all LOHC samples was measured using two vibrating U-tube densimeters from Anton Paar at ambient pressure. The model DMA 5000 M was used in a T range from (283.15 to 363.15) K in steps of 10 K, and the model DMA 4200 M was employed from (298.15 to 473.15) K in steps of 25 K. The DMA 5000 M was adjusted with double-distilled water and air, resulting in an expanded ($k = 2$) relative uncertainty of $U_{\mathrm{r}}(\rho) = 0.0002$, while $U(T) = 0.01$ K according to the manufacturer. The calibration of the DMA 4200 M was carried out following the approach described in Ref. [44]. For this, air and the reference standard APDENA (Paragon Scientific, lot number 4240801, expanded ($k = 2$) relative uncertainty of the certified density data is 0.0001) were used at 293.15 K and from (298.15 to 423.15) K in steps of 25 K, while air and *n*-dodecane (Tokyo Chemical Industry, lot 4RYEG, purity 0.999 according to GC analysis as given in the certificate of analysis) were employed at (448.15 and 473.15) K. Considering the data measured for the APDENA standard and *n*-dodecane by both densimeters as well as the reference data for *n*-dodecane from Lemmon and Huber [45], an expanded relative ($k = 2$) uncertainty of $U_{\mathrm{r}}(\rho) = 0.001$ was concluded for the DMA 4200 M over the complete T range, while $U(T) = 0.03$ K according to the manufacturer. Before filling new samples in either instrument, measurements with deionized water and air were routinely performed at 293.15 K to check the validity of the adjustments. Each reported data set for the LOHC samples studied is the average from measurements with at least two fillings of each densimeter, where the corresponding data agreed clearly within the uncertainties of the instruments. The maximum relative deviation of data measured with the DMA 5000 M from those obtained with the DMA 4200 M for the same sample and T was 0.0002 and, thus, did not exceed the measurement uncertainty of the former instrument. After measurements at elevated T, which were typically completed after about (3 and 4) h for the DMA 5000 M and the DMA 4200 M, check measurements at lower T were frequently performed to ensure that any potential sample changes do not influence the reported data.

2.3 Guarded Parallel-Plate Instrument (GPPI) – Thermal Conductivity

A steady-state guarded parallel-plate instrument (GPPI) was used for the measurement of λ of GBL, BDO, and their mixtures at ambient p of 0.1 MPa. A comprehensive description of the instrument and its operation can be found in reference [46]. In the following, only the fundamental principles and experimental conditions relevant for the present study are described.

The working principle of the GPPI is based on the experimental realization of the ideal one-dimensional form of Fourier's law of heat conduction for a planar sample according to

$$\dot{Q}_{\mathrm{cond}} = \lambda A \frac{\left(T_{\mathrm{hot}} - T_{\mathrm{cold}}\right)}{s}. \tag{1}$$

Based on the determination of the heat flow $\dot{Q}_{\mathrm{cond}}$ caused by pure thermal conduction through the sample layer, the temperature difference between the two outer parallel surfaces of the sample $\Delta T = T_{\mathrm{hot}} - T_{\mathrm{cold}}$, the adjusted thickness of the sample layer s, and the heat transfer area A, the thermal conductivity of the sample λ can be obtained. In the GPPI used, T_{hot} and T_{cold} are determined via T measurements inside the upper heating and the lower cooling plate made of copper, where calibrated Pt-100 Ω resistance probes are used for all T measurements relevant for data evaluation. The measured heat flow $\dot{Q}_{\mathrm{exp}}$ relates to the electrical power dissipated in the resistance heating elements integrated in the heating plate and guided through its lower surface of area A into the sample. $\dot{Q}_{\mathrm{exp}}$ can comprise additional contributions from heat leakage, convection, and/or radiation. The specific design of the used GPPI suppresses heat leakage and convection to a minimum, which allows to assume their contributions to $\dot{Q}_{\mathrm{exp}}$ to be negligible [46]. The contribution of heat transfer due to radiation on $\dot{Q}_{\mathrm{exp}}$ needs to be considered for GBL, BDO, and their mixtures as partially absorbing fluids. For a corresponding estimation, the method proposed by Braun et al. [47] was employed as described in detail by Rausch et al. [48]. This step requires the refractive index of the fluid, which was measured at T from (293.15 to 363.15) K at the sodium vapor line (n_{D} at $\lambda_{\mathrm{D}} = 589.3$ nm) using an Abbe refractometer (NAR-2 T from ATAGO). The additionally needed infrared spectra were measured with a Fourier transform infrared spectrometer (FT/IR-4100 from JASCO) for wave numbers λ ranging from (700 to 4000) cm^{-1} and a layer thickness of $s_0 = 1$ µm at $T = 293$ K.

λ of all samples was measured with an adjusted s of (2.12 ± 0.02) mm ($k = 2$). The average T in the fluid layer was set from (283.15 to 363.15) K in steps of 10 K, where ΔT was maintained at (3.5, 4.0, and 4.5) K and the individual resulting values for λ were averaged. After each measurement, flushing with ethanol and deionized water as well as applying vacuum was used to clean and dry the sample layer, which was then filled with the next liquid sample of interest. Based on propagation calculations, the expanded ($k = 2$) relative uncertainty of the measured data for λ can be specified with $U_r(\lambda) = 0.02$, which is confirmed by frequent check measurements with the reference fluid water. After the experimental run for a given sample, which lasts in total about 90 h and is usually completed at the highest T of 363.15 K, a repetition measurement was conducted at $T =$ (293.15 or 303.15) K. In all cases, the values for λ from the repetition agreed with the initial data within the stated uncertainty, which confirms the stability of the samples during the measurement series up to 363.15 K.

2.4 Dynamic Light Scattering (DLS)

DLS was applied for the determination of a and D_{11} of the LOHC samples at a p of about 0.2 MPa. Detailed explanations of the principles of DLS and its experimental realization for the determination of various thermophysical properties of pure fluids and binary fluid mixtures can be found in the literature, see, e.g., Refs. [49–53]. In the following, only the information relevant for the present study is given.

DLS analyzes the time-dependent intensity of light scattered by a fluid exposed to coherent laser light at macroscopic thermodynamic equilibrium. The scattered light is modulated by microscopic hydrodynamic fluctuations in T or entropy, p, and, in binary mixtures, chemical potential μ or concentration c. As the relaxation of these microscopic fluctuations or gradients is governed by the same laws as those valid for systems subjected to macroscopic gradients according to Onsager's regression hypothesis [54], DLS allows access to several thermophysical properties without the need for calibration. The data analysis is performed in the time domain by the calculation of a normalized second-order correlation function (CF), $g^{(2)}(\tau)$, with respect to the correlation time τ. Neglecting the fluctuations in p, the CF for a binary fluid mixture in the heterodyne detection scheme, where much stronger reference light is coherently superimposed onto the scattered light, is given by a sum of two exponentials via

$$g^{(2)}(\tau) = b_0 + b_t \exp(-|\tau| / \tau_{C,t}) + b_c \exp(-|\tau| / \tau_{C,c}) \tag{2}$$

In Eq. (2), b_0, b_t, and b_c are experimental constants. The decay times $\tau_{C,t}$ and $\tau_{C,c}$ represent the mean lifetimes of fluctuations in T and c and are related to a and D_{11} via

$$\tau_{C,t} = (aq^2)^{-1} \text{ and } \tau_{C,c} = (D_{11}q^2)^{-1} \tag{3}$$

These relations are valid for the mixtures investigated within this work since coupling effects between the two hydrodynamic modes can be safely neglected [55, 56].

The modulus of the scattering vector q is given by the refractive index of the fluid n_{fluid}, the laser wavelength in vacuum λ_0, and the scattering angle Θ_{S} according to

$$q = \frac{4\pi n_{\mathrm{fluid}}}{\lambda_0} \sin\left(\frac{\Theta_{\mathrm{S}}}{2}\right) \tag{4}$$

The Snell-Descartes law allows the determination of Θ_{S} via n_{fluid} and the incident angle Θ_{I} which is adjusted and measured outside the sample cell.

The experimental and electronic setup is the same as in our previous works [55, 57–60]. The scattered light is detected using two photomultiplier tubes (PMTs) operated in a pseudo-cross correlation scheme. The CFs were recorded simultaneously by a linear-tau correlator (LTC) and a multiple-tau correlator (MTC). While the MTC features a quasi-logarithmic spacing between the correlator channels and provides a fixed time structure in a broad time range, the LTC exhibits a constant time spacing between the correlator channels which can be adjusted by changing the sampling time so that the resolution of the signal contribution of interest is optimized. In pure fluids, Eq. (2) is reduced to a single exponential function with decay time $\tau_{\mathrm{C,t}}$, allowing access to a only. An example of a CF recorded by the LTC, where the thermal and the mass mode could be resolved simultaneously, is shown in Fig. 1 for the binary mixture with $x_{\mathrm{GBL}} = 0.75$ at $T=372.68$ K and $p=0.165$ MPa. Here, a superimposed disturbance in the long-time range, which may be caused, for example, by particulate impurities or fluid structures in the sample and/or dust on optical components, was already subtracted from the measured CF. Such a disturbance was visible in almost all CFs recorded within this work. To reliably account for such long-term contributions, an additional first- and/or second-order polynomial with

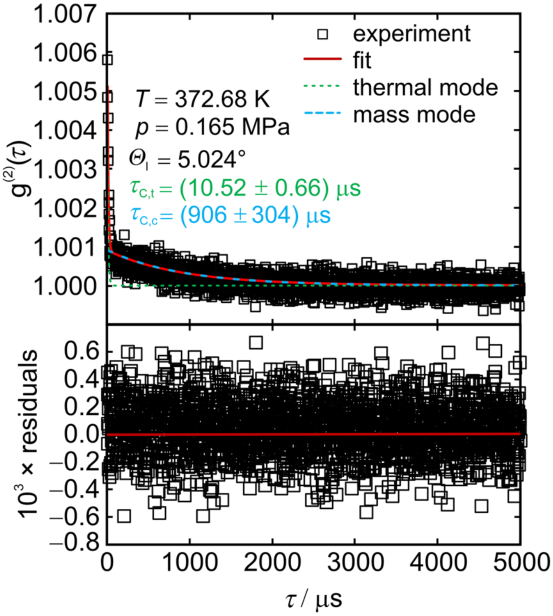

Fig. 1 CF recorded by the LTC for the binary mixture with $x_{\mathrm{GBL}} = 0.75$ at $T = 372.68$ K, $p=0.165$ MPa, and $\Theta_{\mathrm{I}}=5.024°$ (top) and the residuals from the fit (bottom). The solid red line represents the global fit according to Eq. (2). The signals related to a and D_{11} are shown by the green dotted and the blue dashed line, respectively

respect to τ was added to Eq. (2). The residual plot in the lower part of Fig. 1 shows that the theoretical fit model based on Eq. (2) with two exponentials represents the measured CF well. The faster mode can be attributed to $\tau_{\mathrm{C,t}}$ and, thus, to a with a value of $8.88 \times 10^{-8}\ \mathrm{m^2 \cdot s^{-1}}$, which is in the typical range of the thermal diffusivity of organic solvents [58, 61, 62]. The slower mode related to $\tau_{\mathrm{C,c}}$ gives access to D_{11} with a value of $1.03 \times 10^{-9}\ \mathrm{m^2 \cdot s^{-1}}$, which is about two orders of magnitude smaller than a. The assignment of the modes to the transport properties was validated by their T dependence as shown in Sect. 3.5.

Simultaneous access to a and D_{11} by the analysis of a single CF recorded by the LTC was, however, not possible for certain state points. In this case, the two modes were evaluated separately. This situation was particularly pronounced in mixtures with low x_{GBL} and/or at low $T = (298$ and $323)$ K, where D_{11} is relatively small compared to a. Under these conditions, Θ_{I} and the sampling time of the LTC were adjusted to resolve the thermal and mass modes individually in the short- and long-time range. In detail, the thermal mode is analyzed at smaller Θ_{I} and shorter sampling times, while the mass mode is studied at larger Θ_{I} and larger sampling times. Such two cases are depicted in Section S1 of the Supplementary Information for the binary mixture with $x_{\mathrm{GBL}} = 0.75$.

For applying the working equations given in Eq. (3), it is necessary to confirm that the contributions in the observed signal are indeed related to hydrodynamic fluctuations. For this purpose, the hydrodynamic fluctuation theory needs to be employed [63]. The latter states that the relationship between the inverse of the mean lifetime of the fluctuations and the squared modulus of the scattering vector has to be linear and cross the origin, where the slope represents the magnitude of the respective diffusivity, cf. Equation (3). Figure 2 shows this relationship by means of example for the binary mixture with $x_{\mathrm{GBL}} = 0.50$ at $T = 348.13$ K and

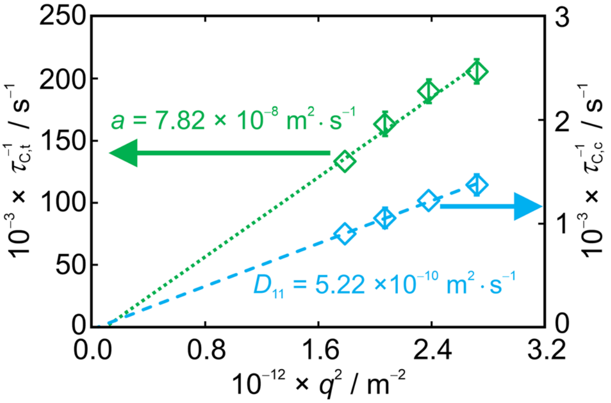

Fig. 2 Inverse of the mean lifetime of fluctuations in temperature $\tau_{\mathrm{C,t}}^{-1}$ or concentration $\tau_{\mathrm{C,c}}^{-1}$ as a function of the squared modulus of the scattering vector q^2 for the binary mixture with $x_{\mathrm{GBL}} = 0.50$ at $T = 348.13$ K and $p = 0.243$ MPa. Symbols represent the experimentally determined values and error bars indicate their expanded experimental uncertainties ($k = 2$), which are shown only if they are larger than the symbols. The green dotted and the blue dashed lines represent the linear fits of $\tau_{\mathrm{C,t}}^{-1}$ and $\tau_{\mathrm{C,c}}^{-1}$, respectively

$p = 0.243$ MPa. Therein, the open markers indicate the measurement results obtained at varying q, whereas the dotted green line and the dashed blue line represent the fits for ${\tau_{C,t}}^{-1}$ and ${\tau_{C,c}}^{-1}$ as a function of q^2. In the fitting process, the data points were weighted according to the inverse of their relative uncertainties, and no constraint was imposed for the fit to pass through the origin. Taking the expanded experimental uncertainties into account, both fit lines capture the data points and cross the origin, which demonstrates that the respective modes result from hydrodynamic fluctuations. For the DLS measurements, a stainless-steel sample cell with four optical accesses and a total volume of 32 mL was filled with approximately 20 mL of the sample. Afterward, vacuum was shortly applied using an oil-sealed vacuum pump to purge the vapor phase inside the cell. To prevent any contamination or uptake from the surroundings, helium was injected into the sample cell to maintain p of about 0.2 MPa that is slightly higher than the ambient pressure. Due to the extremely low solubility of helium in liquids at this low p, it can be assumed that its presence has no significant impact on D_{11} and a. During the DLS measurements, T and p were continuously monitored with a Pt-100 Ω resistance probe and a pressure transducer with absolute uncertainties ($k = 2$) of 20 mK and 8 kPa of the sensors used. For each thermodynamic state point, the a and D_{11} values considered for reporting in data tables are the averages of 8 to 12 diffusivity results obtained from independent CFs recorded at different Θ_I by the LTC and MTC and weighted by the inverse of their relative uncertainties. The same weighting scheme is applied for the calculation of the reported uncertainties in form of the double standard deviation of the individual diffusivities obtained for a given state point on a confidence level of 0.95. The reported T values in the data tables represent the mean values, averaged over the complete measurement period at a given state point. The stated expanded ($k = 2$) uncertainties in T, $U(T)$, and in p, $U(p)$, for a given state point represent the sum of three contributions. The first contribution is the uncertainty in the calibration of the measurement probe. The second one represents the mean stability during the individual recording periods of CFs for the different q. It is the average of the double standard deviations of the T or p data recorded for the different q. The third contribution represents the overall stability at a given state point and is quantified by the double standard deviation of the mean values for T or p at the different q studied for a given state point. To assess the stability of the samples, check measurements were performed typically at $T = (348 \text{ or } 373)$ K after DLS investigations at higher T between (398 and 473) K. The results from these stability studies will be discussed in detail in Sect. 3.1.

2.5 Polarization-Difference Raman Spectroscopy (PDRS)

Raman spectroscopy enables the investigation of mixture composition, including the so-called degree of hydrogenation (DoH) in the case of LOHC systems, after a proper calibration [64, 65]. Furthermore, it can provide helpful insights into fluid structure as given, e.g., in Refs. [66, 67]. In the present study, polarization-difference Raman spectroscopy (PDRS) was applied, as it effectively minimizes or even suppresses the fluorescent contribution to the spectra. The optical setup used for the PDRS investigations is integrated into the DLS setup and is identical to that explained in detail in previous works [65, 68]. In the following, only details relevant for the PDRS investigations on the samples also studied by DLS as well as on further samples used for calibration purposes are given.

PDRS was used for the analysis of molecular vibrations that exhibit primarily symmetric motion. Based on polarized (I_{VV}) and depolarized (I_{HV}) intensity spectra as a function of the Raman shift or wavenumber ν recorded under a scattering angle of 90°, the average isotropic spectrum is obtained as described by Jander et al. [64]. To enhance the visibility in the ν regions of interest, a baseline correction is applied to the isotropic spectra. To determine or check the composition or DoH of the binary mixtures during DLS experiments, a calibration with GBL/BDO mixtures of known composition is required. For the calibration, the two pure fluids and nine binary mixtures, covering in total a x_{GBL} range from 0.00 to 1.00 in increments of 0.10 at $T=(298, 348, \text{and } 373)$ K were studied in quartz cuvettes. The cuvettes were filled with the liquid sample and sealed so that the compositions of the binary mixtures do not change with increasing T. Based on the measurements with a Pt-100 Ω resistance probe placed within the liquid sample, the T stability during these measurements was associated with a maximum double standard deviation of 39 mK.

For the eleven samples studied at 0.1 MPa, the isotropic PDRS spectra are shown in Fig. 3 as a function of ν at a mean temperature of $T=372.98$ K. The main challenge was to identify regions with characteristic Raman signatures for the individual LOHC species in which no contribution from the other species is present. For GBL, a characteristic Raman peak attributable to the C=O stretching of the ketone group mode is located at $\nu \approx 1770$ cm^{-1}, where no contribution from BDO is present. For BDO, the evaluation of the mode related to the two C–O groups at $\nu \approx 1080$ cm^{-1} is more challenging due to overlapping signal contributions from neighboring peaks originating from GBL. The intensities of both peaks show no T dependency in the

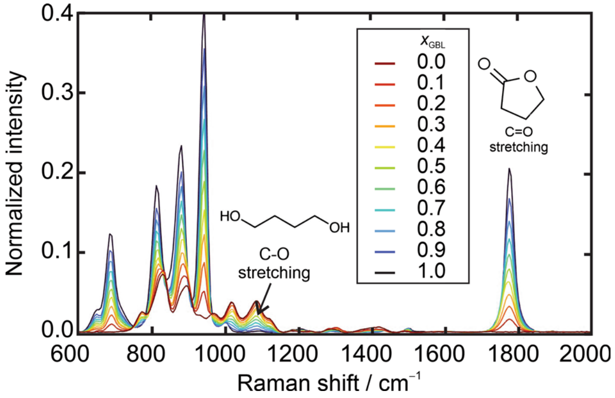

Fig. 3 Baseline-corrected isotropic Raman spectra for BDO, GBL, and their binary mixtures at $T=372.98$ K at 0.1 MPa in the Raman-shift range relevant for the calibration. The spectra are normalized to the highest peak which is not shown in the figure. The data points are connected by straight lines for better visualization. For distinguishing the lines related to different sample composition via the line color, the reader is referred to the online version of this paper

normalized spectra, which is an important criterion for the calibration experiments. The signal intensities in form of the peak areas underneath the Raman peaks characteristic for GBL (I_{GBL}) and BDO (I_{BDO}) were determined on the basis of a Gaussian peak-fit algorithm detailed in Ref. [69]. The C=O peak characteristic for GBL could be fitted with a single Gaussian function. Since the C–O peak associated with BDO overlaps with other peaks, which also overlap with their neighbors, a fit of eleven Gaussian peaks from $\nu = (650 \text{ to } 1150)\ \mathrm{cm}^{-1}$ was required. After successful separation of the individual peaks, the corresponding values for I_{BDO} and I_{GBL} could be obtained. The uncertainties for I_i were calculated by relating the residuals from the fitting process to the integrated area, i.e., $U(I_i) = I_{\mathrm{residual},i} / I_{\mathrm{fit},i}$. As a result, the ratio of the respective peaks, also known as intensity ratio, was calculated as

$$I_{\mathrm{r}} = \frac{I_{\mathrm{GBL}}}{I_{\mathrm{BDO}}} \tag{5}$$

The uncertainty of I_{r}, $U(I_{\mathrm{r}})$, was calculated using error propagation in quadrature using $U(I_i)$. With I_{r} and the gravimetrically determined amount fractions x_{GBL}, the calibration factor K in the relation [64, 65]

$$x_{\mathrm{BDO}} = 1 - x_{\mathrm{GBL}} = \frac{1}{1 + I_{\mathrm{r}}K} \tag{6}$$

can be determined by a fitting process. In the latter, the sum of the inverse relative uncertainties in I_{r} and x_{BDO} is employed for weighting. The value for K was obtained from the calibration measurements with the nine binary mixtures, which are shown in Fig. 3. With this information, it was also possible to monitor the composition and the stability of the samples during the DLS measurements.

3 Results and Discussion

Since experimental observations and routinely performed check measurements indicated that the samples studied undergo changes under specific conditions, these aspects are summarized before the presentation of the experimental results. Regarding the latter, the discussion of the calibration of PDRS for the optical measurement of the mixture composition is followed by that of the measurement results for ρ, λ, a, and D_{11}. The discussion of these data with respect to the influences of T and composition and of information on derived c_{p} data includes a comparison with corresponding literature data.

3.1 Sample Stability

After each measurement series of λ up to $T = 363.15$ K lasting about 90 h, the initially obtained value at low T could be reproduced clearly within the experimental uncertainty. This shows that in this T range, no measurable change of the sample characteristics seems to occur. This is confirmed by the more sensitive ρ measurements, where similar check measurements after about 4 h indicated stability of all mixtures up to 398.15 K and of the pure GBL and BDO up to the corresponding maximum T of (448.15 and 473.15) K. For the mixtures, check measurements at 348.15 K after measurements at 423.15 K showed slight, yet significant deviations from the results obtained initially at this T, indicating the onset of a change of the sample characteristics. At 448.15 K, no measurements were possible for the mixtures since a continuous drift of the measured oscillation period occurred. Observations related to sample stability in the DLS experiments, which require longer exposure times of the sample to a specific T than the measurement of ρ, are given in detail in section S2 of the Supplementary Information and summarized in the following. After investigations at elevated T of 423 K and above, check measurements for a of pure GBL showed considerable deviations from its initial values as shown in Figure S3. A continuous increase in p was additionally observed during the DLS measurements at 448 K, which could indicate a possible formation of volatile compounds. Furthermore, the onset of a change in the color of the laser beam passing the sample from green to yellowish was observed at 398 K, and became more intense at larger T. The color change is shown by photos given in Figure S4 of the Supplementary Information. On this basis, DLS data measured for the pure GBL are assumed to be reliable up to 398 K. For pure BDO, Figure S5 shows that the result from a check measurement for a at 373 K after studying a maximum T of 398 K agreed with the previous one, but was associated with larger uncertainties. In addition, an increase in p and measurable p fluctuations were observed during the DLS measurements at 498 K. Long-term contributions in the recorded CFs became more pronounced already starting from 448 K. On this basis, it is concluded that corresponding measurements for pure BDO up to 423 K should be reliable. The conclusions from the situation described in detail for the mixture with $x_{\mathrm{GBL}} = 0.25$ in section S2 of the Supplementary Information in connection with Figure S6, where two fillings of the sample cell were studied, also holds for the further mixtures in a similar manner. Here, a series of experiments has shown that the mixtures with $x_{\mathrm{GBL}} = (0.25, 0.50, \text{and } 0.75)$ start to change their characteristics in a noticeable way at 448 K. These changes are mainly reflected in the distinct increase in measurement uncertainties for D_{11} that may be related to instabilities of the sample composition, where this effect increases with increasing exposure time at the corresponding T. At higher T, a continuous increase in p with an approximate average rate of 10 $\mathrm{kPa \cdot h^{-1}}$ and the appearance of long-term contributions in the recorded CFs were additionally observed for the mixtures. On this basis, DLS data measured for the mixtures with $x_{\mathrm{GBL}} = (0.25, 0.50, \text{and } 0.75)$ are assumed to be reliable up to 423 K. Further indications regarding a limited stability of the samples were given by the Raman spectra measured in parallel to the application of DLS. For the mixture with $x_{\mathrm{GBL}} = 0.75$, for example, the C—O stretching domain recorded at 323 K before and after the sample had been studied up to 473 K by DLS exhibited some modification that can be seen in Figure S8. Although no additional peaks appeared that might help to identify further compounds that could be formed at elevated T, different possible corresponding reactions have been proposed in the literature [1, 23, 70]. Here, one prominent example is the potential formation of 4-hydroxybutyl 4-hydroxybutanoate (4-HHB) from the combination of GBL and BDO. Since the analytical identification of such reaction products is out of the scope of our current investigation, the following presentation and discussion of results obtained from the different methods mainly considers the fully reliable data where experimental observations and check measurements did not indicate any significant changes in the sample characteristics. Only such data were considered for the development of correlations. The latter are shown in diagrams by solid lines in the T range considered for their development, while broken lines indicate corresponding extrapolations. To some extent, data related to the T range where changes in the sample composition are suspected are additionally presented. To indicate that these data need to be handled with caution, they are marked with an asterisk in data tables and with broken symbol contours in diagrams.

3.2 Calibration of PDRS

For the calibration of PDRS, the values for x_{BDO} as a function of I_{r} are shown in Fig. 4, where the corresponding data are given in Table S1 of the Supplementary Information. For the three investigated $T=(298, 323, \text{and } 373)$ K, the results determined for I_{r} at a given x_{BDO} agree within expanded uncertainties ($k=2$). The fitting of experimental data to Eq. (6) was performed considering a weighting based on the inverse relative uncertainties of the gravimetrically determined x_{BDO} and I_{r} data. Individual fits were performed for each T, where the resulting values $K(T)$ are 0.3031, 0.2984, 0.3029 for $T=(298, 323, \text{and } 373)$ K, respectively. The $K(T)$ values agree within their fit uncertainties, leading to the conclusion that K is independent of T within the studied T range. Averaging of $K(T)$ and the corresponding fit uncertainties provided on a confidence level of 0.95 leads to a final calibration constant of $K=(0.3015 \pm 0.0053)$. Its use in Eq. (6) yields the solid line in Fig. 4, which indicates the good representation of the data points considered for the fitting procedure.

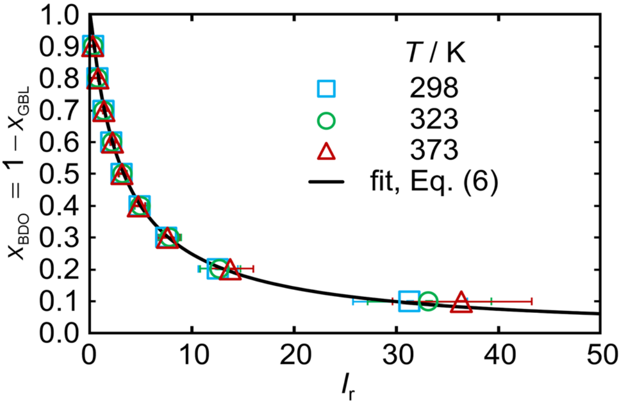

Fig. 4 Calibration results for PDRS showing the gravimetrically determined $x_{\mathrm{BDO}}=(1-x_{\mathrm{GBL}})$ as a function of the intensity ratio I_{r} obtained from the isotropic Raman spectra of the binary mixtures of GBL and BDO from $x_{\mathrm{GBL}}=(0.10 \text{ to } 0.90)$ at three different T. The line represents Eq. (6) with the deduced calibration factor $K=0.3015$

The fit quality is quantified by an average absolute deviation (AAD) and a maximum absolute deviation (MAD) of the gravimetrically determined amount fractions from those calculated based on Eq. (6) of 0.0047 and 0.0164. With the help of K, Eqs. (5) and (6) could be used to monitor the composition of the samples during the DLS measurements at varying T. In general, agreement between x_{GBL} obtained by PDRS and the values determined from the gravimetric mixture preparation was found. Considering the uncertainties of K and I_{r}, no change in the sample composition during the DLS measurement series could be observed by PDRS. Owing to the larger uncertainties in amount fractions obtained by this optical method, the data for x_{GBL} from the gravimetric mixture preparation are used in the following to describe the mixture compositions studied.

3.3 Density

For all systems investigated, the results for ρ measured at $p=0.1$ MPa are summarized in Table 3. Figure 5 represents the measurement results for ρ as a function of T from (283.15 up to 473.15) K. For pure GBL, measurements at $T=473.15$ K were not possible owing to the onset of evaporation. Since for the mixtures, check measurements at 348.15 K after measurements at 423.15 K showed slight, yet significant deviations from the results obtained initially at this T, the data measured at 423.15 K are marked with an asterisk in Table 3 and by broken contours in Fig. 5 to indicate their limited reliability due to an apparent onset of sample instability.

For each system, the complete set of fully valid ρ data was correlated with respect to T by an unweighted fit using a polynomial equation according to

$$\rho_{\mathrm{calc}} = \sum_{i=0}^{n} \rho_i \cdot T^i \tag{7}$$

with $i=(0, 1, \ldots, n)$. While for the binary mixtures, $n=2$ was sufficient to describe the experimental data well, $n=3$ was required for the pure GBL and BDO to ensure that the correlation captures all experimental data within their uncertainties. The respective fitting parameters of Eq. (7) and the average absolute relative deviation (AARD) of the measured ρ values from the fit are summarized in Table 4. Since in all cases, Eq. (7) represents the measurement results within their uncertainties, the correlations are assumed to be associated with expanded ($k=2$) relative uncertainties of $U_{\mathrm{r}}(\rho_{\mathrm{calc}})=(0.0002$ and $0.001)$ for T up to 363.15 K and from there up to the maximum T considered in the correlation procedure, respectively. The maximum AARD of 0.00007 was found for the mixture with $x_{\mathrm{GBL}}=0.50$. For all mixtures, the extrapolation of the correlation beyond 398.15 K illustrated by dashed lines in Fig. 5 agrees with the slightly compromised measurement data at $T=423.15$ K within their uncertainty.

Figure 5 shows the expected decrease of ρ with increasing T from (283.15 to 398.15) K, which is between (7.5 and 10.3)% for pure BDO and pure GBL, respectively. ρ of pure GBL is distinctly larger than that of BDO at the same T, with a relative difference of 11% at $T=293.15$ K. For the binary mixtures of GBL and BDO, the excess molar volume $V_{\mathrm{m}}^{\mathrm{E}}$ was calculated as described in detail in

Table 3 Liquid density ρ of GBL and BDO and their mixtures at different x_{GBL} measured at 0.1 MPa as a function of T.[a]

T / K	ρ / (kg·m^{-3})				
	$x_{\mathrm{GBL}}=0.00$	$x_{\mathrm{GBL}}=0.25$	$x_{\mathrm{GBL}}=0.50$	$x_{\mathrm{GBL}}=0.75$	$x_{\mathrm{GBL}}=1.00$
DMA 5000 M					
283.15	1021.69	1049.94	1078.23	1105.08	1139.20
293.15	1015.59	1042.79	1070.10	1096.09	1129.28
298.15	1012.55	1039.22	1066.03	1091.60	1124.33
303.15	1009.50	1035.64	1061.95	1087.10	1119.38
313.15	1003.41	1028.47	1053.78	1078.10	1109.53
323.15	997.30	1021.26	1045.58	1069.09	1099.69
333.15	991.14	1013.99	1037.33	1060.04	1089.87
343.15	894.89	1006.66	1029.04	1050.98	1080.06
348.15	981.73	1002.97	1024.87	1046.42	1075.17
353.15	978.55	999.24	1020.68	1041.86	1070.26
363.15	972.09	991.73	1012.24	1032.69	1060.45
DMA 4200 M					
298.15	1012.4	1039.2	1066.1	1091.5	1124.4
323.15	997.37	1021.2	1045.6	1069.1	1099.8
348.15	981.79	1003.0	1025.0	1046.5	1075.3
373.15	965.53	984.12	1003.9	1023.5	1050.4
398.15	948.22	964.74	982.28	1000.2	1025.5
423.15	929.85	944.62*	960.37*	976.67*	1000.1
448.15	910.27	–	–	–	974.57
473.15	888.57	–	–	–	–

[a] Data that need to be handled with care owing to slight instabilities are marked with an asterisk (*). The uncertainties $U(T)$ for the DMA 5000 M and the DMA 4200 M are (0.01 and 0.03 K), respectively. The relative uncertainties $U_{\mathrm{r}}(\rho)$ measured by the DMA 5000 M and the DMA 4200 M are (0.0002 and 0.001), respectively. All uncertainties are given on a confidence level of 0.95 (coverage factor $k=2$)

section S4 of the Supplementary Information. Therein, Figure S9 shows that the magnitude of $V_{\mathrm{m}}^{\mathrm{E}}$ in the reasonably accessible T range up to 363.15 K does not exceed 0.3 cm^3·mol^{-1}. This implies that using a corresponding idealized and easily applicable molar volume-based mixing rule employing the correlations for the pure mixture components according to Eq. (7), a maximum deviation of measured from such predicted data of 0.33% results. $V_{\mathrm{m}}^{\mathrm{E}}$ consistently increased with increasing T for all mixtures, where it is mostly negative for the mixture with $x_{\mathrm{GBL}}=0.25$ and always positive for the others. Considering the generally small magnitudes of the $V_{\mathrm{m}}^{\mathrm{E}}$ values and the rather complex nature of interactions in such a polar system, any detailed interpretation of the observed behavior would be rather speculative and is, therefore, not given here.

For the pure LOHC compounds studied, the relative deviations of the present experimental values and of corresponding literature data from ρ_{calc} obtained from the respective correlations according to Eq. (7) developed in this work are shown

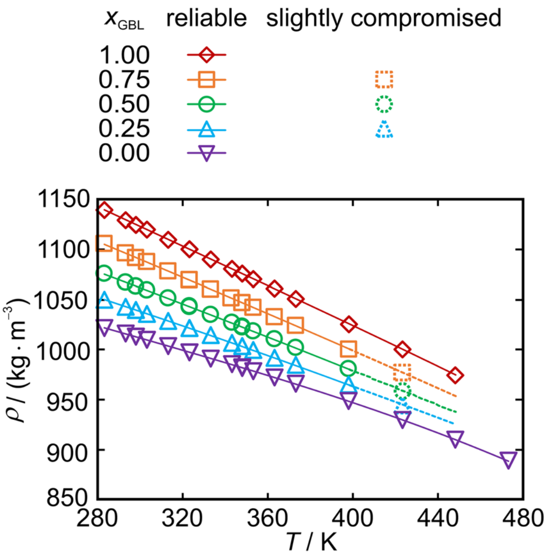

Fig. 5 Experimental data for ρ of the systems studied with varying x_{GBL} as a function of T at 0.1 MPa. Markers with contours of solid and broken lines indicate reliable and slightly compromised measurement data. Solid lines represent the correlations based on Eq. (7), where dashed lines indicate their extrapolation beyond the reliable T range

Table 4 Coefficients of Eq. (7) for the calculation of the liquid density ρ_{calc} as a function of T for GBL and BDO and their binary mixtures

x_{GBL}	ρ_0 / (kg·m^{-3})	ρ_1 / (kg·m^{-3}·K^{-1})	ρ_2 / (kg·m^{-3}·K^{-2})	$10^6\times$ ρ_3 / (kg·m^{-3}·K^{-3})	T range / K	AARD[a]
0.00	1260.91	−1.31597	0.00247449	−2.86633	283.15–473.15	0.000044
0.25	1218.70	−0.495316	−0.000357477	–	283.15–398.15	0.000055
0.50	1281.38	−0.660831	−0.000238207	–	283.15–398.15	0.000069
0.75	1341.68	−0.782978	−0.000187098	–	283.15–398.15	0.000038
1.00	1454.78	−1.33321	0.00109415	−1.13925	283.15–448.15	0.000048

[a] Average absolute relative deviation of the experimental data from the corresponding correlations

in Fig. 6. A comparison with literature data for mixtures of GBL and BDO is not possible owing to the lack of such data.

For GBL, Chen et al. [29] report ρ data between (293.15 and 333.15) K measured by an oscillating U-tube densimeter. Their data are consistent with those measured by Ritzoulis et al. [41] with a vibrating-tube densimeter from (298.15 to 303.15) K, by Ramkumar and Kudchadker [31] with a pycnometer from (298.15 to 343.15) K, and by Al-Azzawi and Awwad [32] with a vibrating-tube densimeter at 303.15 K. The relative deviations of these data sets from the present ones are approximately 0.05% and, for most cases, slightly outside combined uncertainties. Further ρ data for pure GBL were reported by Abdullah and Al-Madafi [30] between (288.15 and 318.15) K, by Vraneš et al. [34] between (293.15 and 323.15) K, and by Krakowiak et al. [35] between (288.15 and 313.15) K that were measured with different vibrating-tube densimeters. In these cases, most reported data agree with the present results within combined uncertainties. All of them are in a total range of

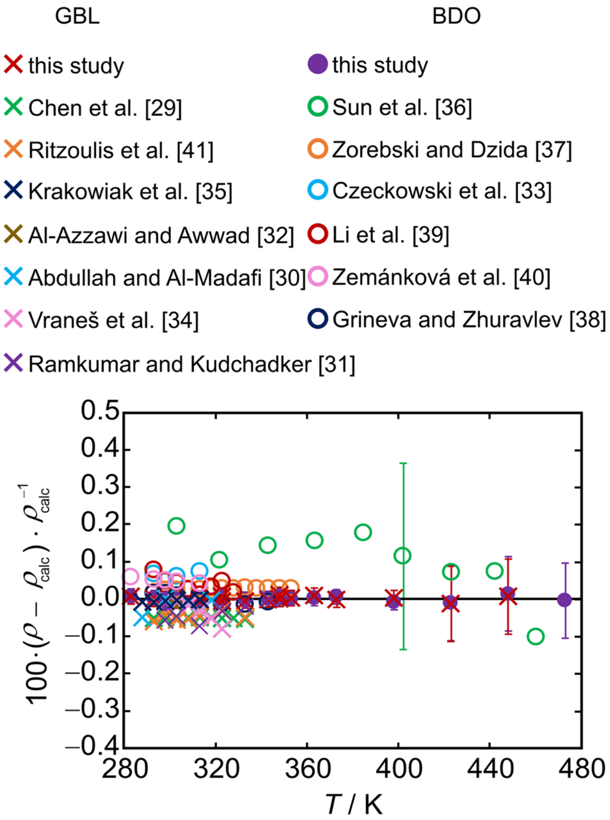

Fig. 6 Relative deviation of ρ data measured for pure GBL and BDO in the present work and taken from the literature from the corresponding correlations according to Eq. (7) as a function of T. Expanded uncertainties ($k = 2$) of the present experimental data are shown as error bars. For the literature data, stated uncertainties are only given exemplarily to ensure legibility as far as the values given in the references are outside the markers. To distinguish the different data sets from the literature via the color of the symbols, please refer to the online version of this work

approximately 0.1% and show a reasonable agreement with the data from the present study, which is the only one that provides density data for GBL at $T > 343$ K.

For BDO, Sun et al. [36] report ρ data between (303.3 and 460.3) K, where the seemingly large deviation from the present results can be related to the uncertainty of 0.25% stated for the high-pressure pycnometer used. Different vibrating-tube densimeters were used by Czeckowski et al. [33] at (293.15, 303.15, and 313.15) K, by Zorebski and Dzida [37] between (293.15 and 353.15) K, and by Zemánková et al. [40] between (283.15 and 313.15) K. In addition, Grineva and Zhuravlev [38] measured between (293.15 and 343.15) K using glass monocapillar pycnometers, while Li et al. [39] employed a Gay-Lussac pycnometer between (293.15 and 328.15) K. Although several of the corresponding data deviate from the present ones slightly outside combined uncertainties, all of them are in a total range of approximately

0.1%, indicating a reasonable agreement. Possible reasons behind the general small deviations for the data for GBL and BDO may be related to sample purities, where the hygroscopic character of these compounds could play a role.

3.4 Thermal Conductivity

For all systems investigated, the results for λ measured at $p = 0.1$ MPa are summarized in Table 5. The data for the refractive index and diagrams for the transmission spectra measured for the evaluation of the radiation contribution to the measured heat flow over the sample layer in the GPPI are given in section S5 of the Supplementary Information. The transmission spectra data are additionally provided as a separate data file. Figure 7 shows all experimental data determined for λ as a function of T in a range between (283.15 and 363.15) K at $x_{\mathrm{GBL}} = (0.00, 0.25, 0.50, 0.75,$ and $1.00)$. It was not possible to determine λ for BDO at $T = 283.15$ K due to solidification of the sample below its melting point of 289.15 K. For each mixture, the experimental data were correlated by an unweighted fit using a linear equation with respect to T according to

$$\lambda_{\mathrm{calc}} = \lambda_0 + \lambda_1 T \tag{8}$$

The respective fit parameters of Eq. (8) and the AARD of the measured λ values from the fit are summarized in Table 6. In all cases, Eq. (8) represents the measurement results within their uncertainties.

Figure 7 shows that λ decreases with increasing T in the range investigated for each x_{GBL}. For pure BDO and pure GBL, λ decreases from (293.15 to 363.15) K by (4.4 and 11)%, meaning that GBL shows a stronger T dependency than BDO. This may be related to the presence of hydrogen bonding between BDO molecules with two

Table 5 Thermal conductivity λ of GBL and BDO and their mixtures at 0.1 MPa for different x_{GBL} as a function of T.[a]

T / K	λ / (mW·m^{-1}·K^{-1})				
	$x_{\mathrm{GBL}} = 0.00$	$x_{\mathrm{GBL}} = 0.25$	$x_{\mathrm{GBL}} = 0.50$	$x_{\mathrm{GBL}} = 0.75$	$x_{\mathrm{GBL}} = 1.00$
283.15	–	197.8	187.7	178.5	172.4
293.15	203.1	193.4	183.5	174.1	169.3
303.15	203.1	192.8	182.7	173.3	168.3
313.15	201.2	190.4	179.6	170.8	166.3
323.15	201.2	189.1	178.9	168.1	163.9
333.15	199.7	188.2	177.7	167.2	161.5
343.15	198.6	186.7	176.7	165.5	158.8
353.15	197.4	187.5	175.5	163.3	156.0
363.15	194.2	184.8	172.5	157.4	150.8

[a] The relative uncertainties of the measured λ are $U_{\mathrm{r}}(\lambda) = 0.02$. T was measured with an expanded uncertainty of $U(T) = 0.01$ K. All uncertainties are given on a confidence level of 0.95 ($k = 2$)

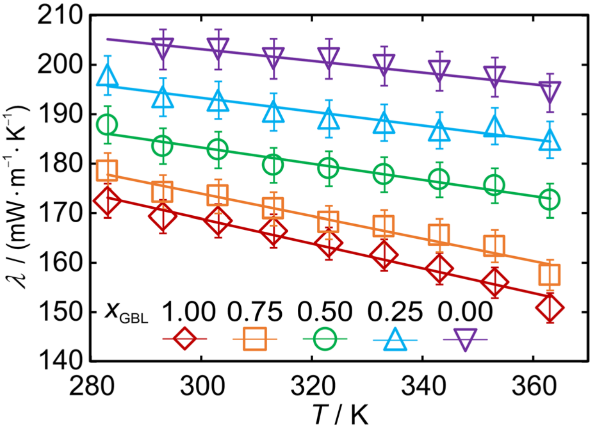

Fig. 7 Experimental data for λ of GBL and BDO and their mixtures at different x_{GBL} as a function of T at 0.1 MPa (markers). The solid lines represent the fits based on Eq. (8)

Table 6 Coefficients of Eq. (8) for the calculation of the thermal conductivity λ_{calc} as a function of T for GBL and BDO and their mixtures at different x_{GBL}

x_{GBL}	λ_0 / (mW·m^{-1}·K^{-1})	λ_1 / (mW·m^{-1}·K^{-2})	T range / K	AARD^a
0.00	238.9	−0.1192	293.15–363.15	0.0035
0.25	235.4	−0.1402	283.15–363.15	0.0048
0.50	232.4	−0.1640	283.15–363.15	0.0040
0.75	241.9	−0.2267	283.15–363.15	0.0058
1.00	243.9	−0.2502	283.15–363.15	0.0056

[a] Average absolute relative deviation of the experimental data from the corresponding fits

hydroxyl groups, which could lead to a weak change of λ with variations in T as seen for, e.g., glycerol [71]. Figure 7 also indicates that λ decreases with increasing x_{GBL} in the T range investigated, where λ of GBL is by 20% smaller than that of BDO at 293.15 K. The concentration dependency can be seen more clearly in Fig. 8, which shows the measured λ data as a function of x_{GBL} at $T=$(293.15 K and 353.15) K. The experimental data for λ of the binary mixtures deviate only slightly from a simple linear amount fraction-based mixing rule, where the deviations are always within the experimental uncertainty of 2%. Therefore, any interpretation of this mixture behavior for λ based on molecular interactions would be speculative.

In Fig. 9, a data comparison for λ of pure GBL and BDO is shown as a function of T using Eq. (8) as a reference in the relative deviation plot. In addition to the present experimental data for both substances, the two data sets for λ of pure BDO reported in literature [27, 28] are included. For GBL, the only available data set determined by Gurevich et al. [72] using the heated-probe method showed a significant average deviation of 87% from the values measured in this work and is, thus, not included in Fig. 9. For pure BDO, Bleazard et al. [27] report experimental λ between (292.2 and 466.1) K from the transient hot-wire (THW) technique with an

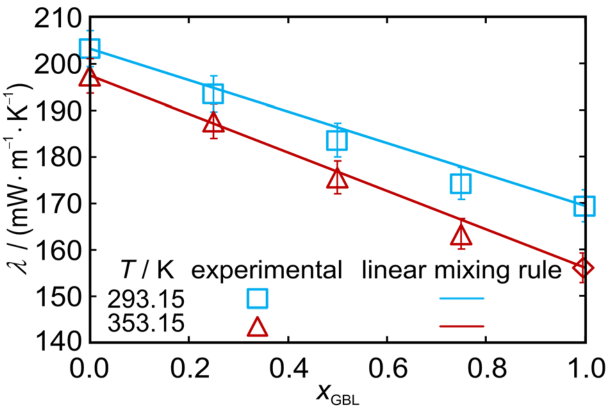

Fig. 8 Experimental data for λ of the studied systems as a function of x_{GBL} at different T at 0.1 MPa. The solid lines indicate a linear amount fraction-based mixing rule using the data for the pure compounds

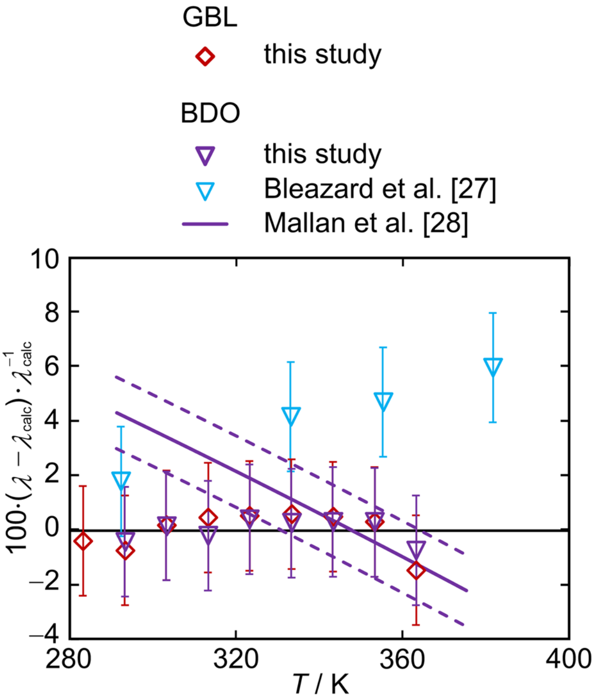

Fig. 9 Relative deviation of measurement results for λ of pure GBL and BDO obtained by the GPPI in this work and reported in the literature [27, 28] from the fit according to Eq. (8) as a function of T. Expanded uncertainties ($k=2$) of the experimental data from this work and from Ref. [27] are shown as error bars. Expanded uncertainties ($k=2$) of the equation specified in Ref. [28] are shown as dashed lines

uncertainty of 2%. The relative deviations between the data from Bleazard et al. [27] and this work are within combined uncertainties up to 333 K and slightly outside combined uncertainties at higher T. Mallan et al. [28] report an equation for λ of BDO between (291.15 and 375.15) K, which was calculated from experimental data obtained with a THW apparatus with an uncertainty of 1.3%. The relative deviations between the data from Ref. [28] and this work are always within about ± 4% and, thus, within combined uncertainties between (313.15 and 363.15) K.

3.5 Thermal and Fick Diffusivity

The results for the thermal diffusivity a and the Fick diffusivity D_{11} from DLS for all investigated systems are summarized in Table 7. The data reported for a specific sample composition and T always represent the results from the measurement performed with the shortest total exposure time of the sample to elevated T, i.e., the results from check measurements are not considered. For the mixture with $x_{\mathrm{GBL}} = 0.25$, the data given for $T = (348$ and $373)$ K are the averages from the corresponding measurements of the two fillings of the sample cell with this mixture. For $T = 423$ K, only the results obtained with the second filling are considered since the corresponding previous exposure time to elevated T was distinctly shorter and the smaller measurement uncertainty visible from the error bars in Figure S6 in the Supplementary Information indicate a better state of this sample.

3.5.1 Thermal diffusivity

Figure 10 shows the results for a as a function of T between (298 and 473) K at $x_{\mathrm{GBL}} = (0.00, 0.25, 0.50, 0.75$, and $1.00)$. The relative expanded uncertainties ($k = 2$) for the reliable a values range from (2.9 to 23) % with an average value of 10%. The uncertainties are indicated as error bars in Fig. 10 if their magnitude is larger than the symbol size. For each pure component and mixture, the reliable experimental data for a obtained in the T ranges where the stability issues discussed in Sect. 3.1 do not apply were correlated with respect to T by a linear fit model according to

$$a_{\mathrm{calc}} = a_0 + a_1 T \tag{9}$$

For the fitting procedure, the individual data points were weighted by the inverse of their relative uncertainty. The respective fit parameters for Eq. (9) and the AARD of the measured a values from the fits are summarized in Table 8. In all cases, Eq. (9) represents the measurement results within their uncertainties. The extrapolation of the correlations beyond the T range considered for the fitting is indicated by the dashed lines in Fig. 10 and describes the measurement results that are probably compromised by changes in the sample within their experimental uncertainties.

Figure 10 indicates that a decreases with increasing T, which agrees with the typical behavior previously reported for organic liquids [51]. This behavior is mainly related to the correspondingly decreasing thermal conductivity, which results from the increasing intermolecular distance going along with the decrease of intermolecular interactions. Particularly at low T, a tends to increase with increasing x_{GBL}. Yet,

Table 7 D_{11} and a together with their expanded relative experimental uncertainties ($k = 2$) for GBL, BDO, and their binary mixtures measured by DLS at different x_{GBL} and T.[a]

T / K	$U(T)$ / K	p / MPa	$U(p)$ / MPa	$10^8 \times a$ / (m^2·s^{-1})	$100 \times U_r(a)$	$10^{11} \times D_{11}$ / (m^2·s^{-1})	$100 \times U_r(D_{11})$
$x_{\mathrm{GBL}} = 0.00$							
298.18	0.03	0.193	0.012	8.0	16	–	–
323.23	0.06	0.149	0.012	6.9	18	–	–
348.11	0.03	0.243	0.014	7.21	12	–	–
372.76	0.04	0.203	0.015	7.17	9.6	–	–
398.26	0.03	0.181	0.013	6.49	12	–	–
423.26	0.16	0.168	0.013	6.35	9.4	–	–
447.94	0.07	0.157	0.013	5.56[*]	6.1	–	–
473.06	0.07	0.213	0.016	5.66[*]	8.1	–	–
$x_{\mathrm{GBL}} = 0.25$							
298.15	0.22	0.119	0.014	8.50	7.6	6.1	20
323.29	0.09	0.163	0.013	8.17	7.1	13.2	27
347.94[b]	0.04[b]	0.194[b]	0.014[b]	7.61[b]	11[b]	38.5[b]	19[b]
372.72[b]	0.03[b]	0.207[b]	0.017[b]	7.3[b]	17[b]	76[b]	13[b]
397.95	0.03	0.163	0.013	7.2	18	105	28
422.25[c]	0.04[c]	0.154[c]	0.014[c]	6.65[c]	8.0[c]	171[c]	17[c]
448.02	0.03	0.221	0.013	6.6[*]	29	243[*]	35
473.13	0.07	0.283	0.025	6.7[*]	21	357[*]	32
$x_{\mathrm{GBL}} = 0.50$							
298.15	0.03	0.194	0.012	8.6	23	7.8	17
323.28	0.03	0.249	0.013	8.2	13	23.3	14
348.13	0.04	0.241	0.017	7.90	10	52.2	12
373.12	0.09	0.172	0.014	7.17	7.6	90	14
397.70	0.04	0.232	0.014	7.06	6.6	141	8.0
422.72	0.05	0.246	0.016	6.84	4.8	197	11
447.60	0.04	0.245	0.015	6.81[*]	12	279[*]	25
472.68	0.04	0.300	0.025	6.35[*]	4.1	326[*]	12
$x_{\mathrm{GBL}} = 0.75$							
298.15	0.03	0.106	0.013	8.59	8.2	19.5	22
322.95	0.04	0.132	0.013	8.34	11	37.3	17
348.20	0.05	0.131	0.013	8.13	6.1	81	20
372.70	0.05	0.165	0.016	7.86	7.2	133	25
397.87	0.11	0.131	0.016	7.7	22	159	20
423.12	0.08	0.199	0.017	7.1	17	199	20
447.87	0.03	0.199	0.015	6.9[*]	16	253[*]	9.0
472.59	0.09	0.232	0.013	6.54[*]	7.3	334[*]	14
$x_{\mathrm{GBL}} = 1.00$							
298.18	0.03	0.157	0.012	9.21	3.3	–	–
323.15	0.03	0.163	0.014	9.04	3.0	–	–
348.03	0.03	0.170	0.014	8.48	4.7	–	–
373.01	0.03	0.179	0.013	7.91	3.1	–	–

Table 7 (continued)

T / K	$U(T)$ / K	p / MPa	$U(p)$ / MPa	$10^8 \times a$ / (m^2·s^{-1})	$100 \times U_r(a)$	$10^{11} \times D_{11}$ / (m^2·s^{-1})	$100 \times U_r(D_{11})$
397.67	0.06	0.131	0.014	7.35	2.9	–	–
423.22	0.04	0.154	0.013	6.93*	4.4	–	–
448.31	0.04	0.201	0.014	6.49*	4.3	–	–
473.22	0.06	0.182	0.012	6.01*	2.7	–	–

[a] Data that are probably influenced by sample changes are marked with an asterisk (*). The estimated absolute expanded uncertainty of x_{GBL} determined according to the gravimetric sample preparation is 0.000003. The reported values for T and p are mean values averaged over the complete measurement period at a given state point. The respective uncertainties $U(T)$ and $U(p)$ account for the uncertainties of the measurement probes as well as stabilities observed during the measurements at a given state point. Details are given in Sect. 2.4. The reported values for a and D_{11} at a given state point are mean values of the individual results obtained at different q with the different correlators, considering a weighting scheme based on their inverse relative uncertainties. The uncertainties $U_r(a)$ and $U_r(D_{11})$ at a given state point are the double standard deviations of the individual diffusivities calculated using the same weighting scheme. All uncertainties are given on a confidence level of 0.95 ($k = 2$)

[b] Average from the data obtained with the two fillings of the measurement cell

[c] Data from the measurement series with the second filling of the measurement cell

a clear influence of the composition on a cannot be resolved considering the measurement uncertainties.

3.5.2 Fick Diffusivity

The results for D_{11} from DLS for all investigated systems are shown in Fig. 11 as a function of T between (283 and 473) K for the mixtures with $x_{GBL} = (0.25, 0.50, \text{and } 0.75)$. The relative expanded ($k = 2$) uncertainties of reliable D_{11} data in the T regime up to 423 K range from (8 to 28)% with an average value of 18%. For each mixture, the reliable data were correlated by the Vogel–Fulcher–Tammann (VFT) equation with respect to T according to

$$D_{11,\text{calc}} = D_{11,0} \exp\left(\frac{B}{T - T_{\text{VFT}}}\right) \tag{10}$$

For the fitting procedure, the individual data points were weighted by their inverse relative uncertainties. The respective fit parameters for Eq. (10) and the AARD of the measured D_{11} values from the fit are summarized in Table 9. In all cases, Eq. (10) represents the measurement results within their uncertainties. An extrapolation of the fit lines based on Eq. (10) to larger T is shown by the dashed lines in Fig. 11 and still captures the probably compromised measurement results within their uncertainties.

As can be seen in Fig. 11, D_{11} increases with increasing T for all mixtures, which is expected due to the increasing kinetic energy and dynamics of the molecules with

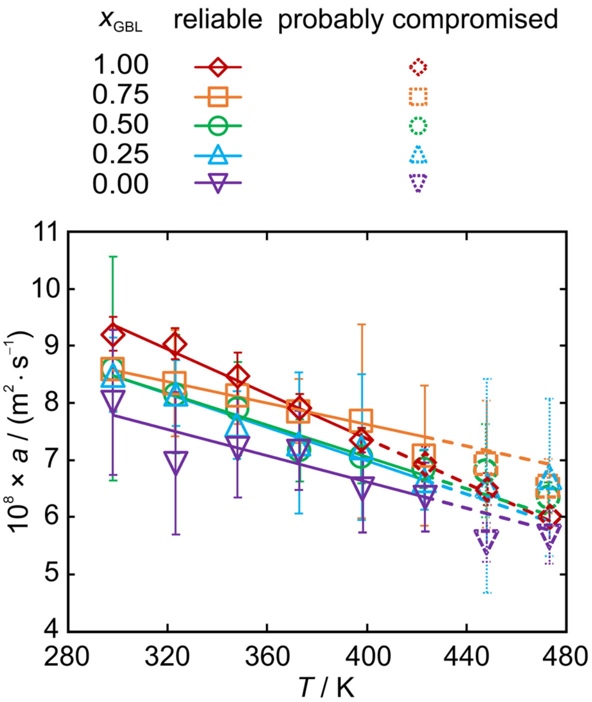

Fig. 10 Experimental data for the thermal diffusivity a of GBL, BDO, and their mixtures with varying x_{GBL} as a function of T at about 0.2 MPa. Open markers indicate reliable a data, whereas the markers with broken contour indicate a data at elevated T that are probably compromised. The solid lines represent the correlation of the data based on Eq. (9), while broken lines indicate their extrapolation. Error bars represent expanded experimental uncertainties ($k = 2$) and are shown only if they are larger than the symbol sizes

Table 8 Fitting coefficients for Eq. (9) for the calculation of the thermal diffusivity a_{calc} as a function of T, the considered T range, and the average absolute relative deviation (AARD) of the experimental results from the fit for GBL, BDO, and their mixtures at different x_{GBL}

x_{GBL}	$10^7 \times a_0$ / ($m^2 \cdot s^{-1}$)	$10^{10} \times a_1$ / ($m^2 \cdot s^{-1} \cdot K^{-1}$)	T range / K	AARD[a]
0.00	1.11	−1.11	298–398	0.028
0.25	1.29	−1.47	298–423	0.011
0.50	1.28	−1.43	298–423	0.013
0.75	1.14	−0.932	298–423	0.040
1.00	1.53	−1.97	298–423	0.011

[a] Average absolute relative deviation of the experimental data from the corresponding fits

rising T. To investigate the influence of the composition on D_{11}, the same results are shown in Fig. 12 as a function of x_{GBL} at different T. D_{11} increases with increasing x_{GBL} for a given T. A more pronounced relative increase can be observed for the lower T. For instance, at $T = 298$ K, D_{11} at $x_{GBL} = 0.75$ is approximately three times higher than the value at $x_{GBL} = 0.25$, whereas at $T = 398$ K, this difference reduces to an about 1.5-fold

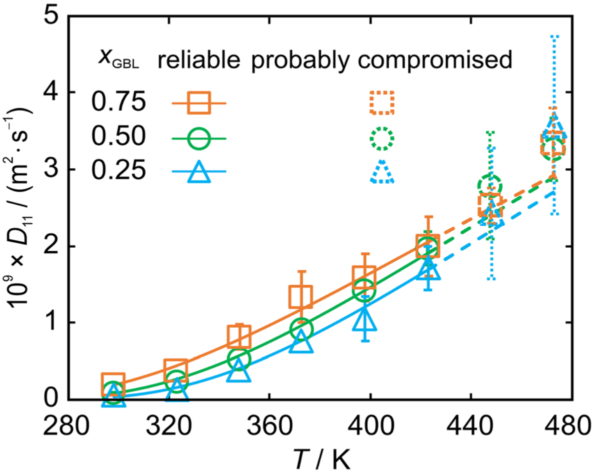

Fig. 11 D_{11} from DLS for binary mixtures of GBL and BDO with varying x_{GBL} as a function of T at about 0.2 MPa. Open markers with solid boundaries indicate reliable data, whereas markers with broken contours indicate that the data need to be handled with caution. The solid lines show the correlation of the data based on Eq. (10), while the dashed lines indicate their extrapolations. Error bars represent expanded ($k=2$) uncertainties and are shown only if they are larger than the symbol sizes

Table 9 Fitting coefficients for Eq. (10) for the calculation of the Fick diffusivity $D_{11,calc}$ as a function of T for the mixtures of GBL and BDO at different x_{GBL}

x_{GBL}	$10^{10}\times D_{11,0}$ / (m^2·s^{-1})	B / K	T_{VFT} / K	T range / K	AARD[a]
0.25	164.66	−459.16	223.54	298–423	0.19
0.50	169.67	−456.28	214.28	298–423	0.05
0.75	154.32	−443.69	202.66	298–423	0.11

[a] Average absolute relative deviation of the experimental data from the corresponding fits

increase. These trends can be rationalized by comparing the dynamic viscosities of pure GBL and pure BDO from the literature [29, 36]. At $T=298$ K, GBL and BDO exhibit values of (1.72 and 71.36) mPa·s, while at $T=398$ K, their viscosities decrease to (1.32 and 2.33) mPa·s. The distinctly decreasing relative difference between the viscosities of GBL and BDO with increasing T agrees with the corresponding behavior of D_{11} for their mixtures. To the best of our knowledge, there are no D_{11} data available in the literature that could be used for comparison.

3.6 Isobaric Heat Capacity

Using the correlations for a, λ ,and ρ according to Eqs. (7), (8), and (9), the isobaric heat capacity c_p of GBL, BDO, and their binary mixtures can be calculated according to

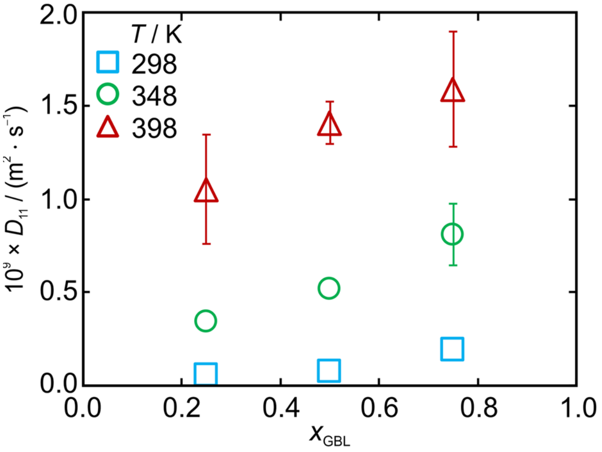

Fig. 12 D_{11} from DLS for binary mixtures of GBL and BDO as a function of x_{GBL} at different T. Error bars represent expanded ($k = 2$) uncertainties and are shown only if they are larger than the symbol sizes

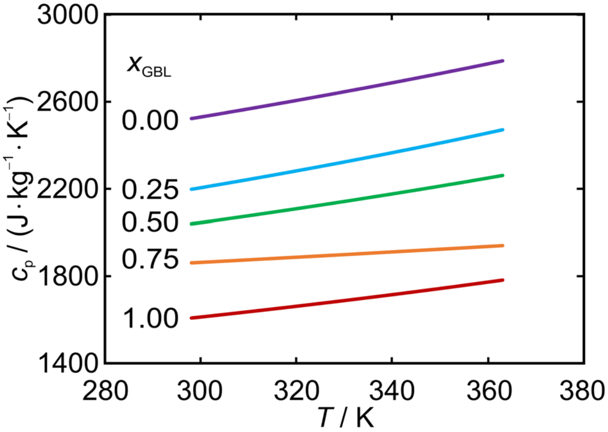

Fig. 13 Isobaric heat capacity c_p of GBL, BDO, and their mixtures with varying x_{GBL} as a function of T at 0.1 MPa calculated from Eq. (11) based on the correlations of the experimental data obtained in this work

$$c_p = \frac{\lambda}{a\rho} \tag{11}$$

In Fig. 13, the calculated c_p values are shown as solid lines as a function of T between (298.15 and 363.15) K. The upper T limit of 363.15 K was defined according to the upper limit of the GPPI measurements. The relative expanded ($k = 2$) uncertainties $U_r(c_p)$ are calculated from propagation calculations in quadrature considering the average relative uncertainties of the measured λ, a, and ρ

data for each system, where the uncertainty in a is the dominant contribution. The final values for $U_r(c_p)$ are listed in Table 10 and are between 0.04 and 0.14. It can be seen from Fig. 13 that c_p shows an increasing trend with increasing T as common for organic liquids. Furthermore, c_p of BDO is approximately 60% larger than that of GBL over the whole T range considered.

To obtain simple equations that describe the nearly linear T-dependent behavior of c_p in the considered T range, c_p data were calculated in steps of 5 K and correlated with respect to T according to

$$c_{p,calc} = c_{p,0} + c_{p,1}T \tag{12}$$

The respective fit parameters of Eq. (12) are given in Table 10. The AARD of the fitted data points calculated from the individual correlations for λ, a, and ρ from $c_{p,calc}$ also given in the table do not exceed 0.0011, which is clearly less than $U_r(c_p)$.

In Fig. 14, available literature data for c_p of pure GBL and BDO are compared with the c_p data calculated from Eq. (11). For the latter data, the relative expanded ($k = 2$) uncertainties $U_r(c_p)$ are shown as dotted lines. For pure GBL, Lebedev and Yevstropov [42] report experimental c_p data from (218.75 to 328.65) K from an adiabatic calorimetric cryostat with an uncertainty of 0.25%. These values agree with the present data within the uncertainties of the latter with a maximum relative deviation of 3.0% in the T range investigated. In addition, c_p of GBL was calculated by Gurevich et al. [72] using experimentally determined values of ρ and λ in Weber's equation in a T range between (243.15 and 373.15) K with an uncertainty of 13%. These data show an average deviation of 111% from the c_p values determined in the present work and are, thus, not shown in Fig. 14. For pure BDO, Zorebski and Góralski [43] provide experimental c_p data between (293.15 and 353.15) K obtained with a differential scanning calorimeter with an uncertainty of 0.25%. Their data agree with the present results within the uncertainties of the latter and exhibit a maximum relative deviation of 13% in the T range investigated.

Table 10 Coefficients of Eq. (12) for the calculation of $c_{p,calc}$ as a function of T for GBL, BDO, and their mixtures at different x_{GBL}

x_{GBL}	$10^7 \times c_{p,0}$ / ($J \cdot kg^{-1} \cdot K^{-1}$)	$10^{10} \times c_{p,1}$ / ($J \cdot kg^{-1} \cdot K^{-2}$)	T range / K	$100 \times U_r(c_p)^a$	AARD^b
0.00	1297.1	4.2840	298.15–363.15	14	0.0009
0.25	942.62	4.1907	298.15–363.15	11	0.0011
0.50	1010.8	3.4279	298.15–363.15	11	0.0009
0.75	1499.9	1.2072	298.15–363.15	12	0.0001
1.00	796.30	2.7044	298.15–363.15	3.9	0.0010

[a] The relative expanded ($k = 2$) uncertainties $U_r(c_p)$ of the $c_{p,calc}$ data calculated from Eq. (11) were determined by propagation calculations in quadrature considering the average relative uncertainties of the input parameters ρ, λ, and a

[b] Average absolute relative deviation of c_p calculated from Eq. (11) from the corresponding fits

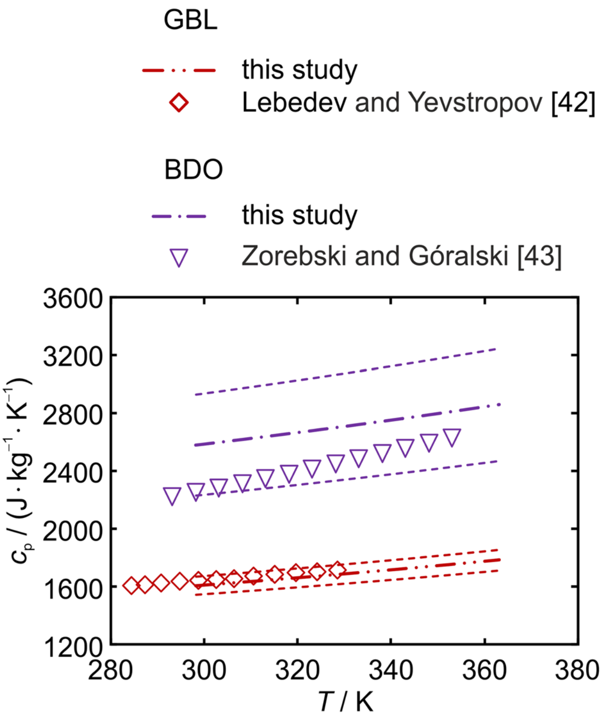

Fig. 14 Isobaric heat capacity c_p of GBL and BDO as a function of T at 0.1 MPa calculated from Eq. (11) based on the correlations of the experimental data obtained in this work. Dotted lines represent the expanded ($k=2$) uncertainties obtained using the average uncertainties for a, λ, and ρ via propagation calculations in quadrature. For comparison, available literature data as described in the text are depicted

4 Conclusions

This work presents a comprehensive experimental investigation of D_{11}, a, λ, and ρ of the promising and upcoming LOHC system based on GBL and BDO for varying x_{GBL} of 0.00, 0.25, 0.50, 0.75, and 1.00 over a wide T range up to 473 K at about 0.1 MPa. For the thermophysical property research, DLS and conventional methods were employed. Furthermore, a calibration of PDRS for the optical determination of the mixture composition was performed. Experimental observations, Raman spectra, and systematically performed check measurements indicated system- and method-specific T ranges in which a sound stability and, thus, reliability of the reported data can be concluded. These ranges are up to $T=423$ K for pure BDO, yet only up to about 398 K for pure GBL and its mixtures with BDO. ρ determined by a vibrating-tube densimeter agrees reasonably with the available literature data for the pure compounds. For the mixtures, the derived excess molar volumes change from negative to positive values with increasing x_{GBL}, indicating a complex interaction between the polar chemicals. λ determined by a GPPI increases with decreasing x_{GBL}, where weak negative deviations from a simple amount fraction-based mixing rule are observed. Using DLS, it was possible to access a and D_{11} simultaneously with average uncertainties ($k = 2$) of (10 and 18)%, where corresponding measurement data were not available in the literature so far. While no clear composition dependence of a could be resolved, D_{11} increases significantly with increasing x_{GBL}, which can be connected to the lower dynamic viscosity of GBL compared to BDO. T-dependent correlations of the experimental data for ρ, a, and λ could be employed in the range between (298.15 and 363.15) K to deduce c_{p}, which increases with increasing T and decreasing x_{GBL}. The present results for λ and c_{p} agree well with the few experimental literature data available for pure GBL and BDO. Besides extending the database of thermophysical properties and giving insights into their T and composition dependencies, the results presented in this work provide a valuable basis for future investigations on further process-relevant properties, where also the influence of H_2 will be considered for this promising LOHC system.

Supplementary Information The online version contains supplementary material available at https://doi.org/10.1007/s10765-025-03694-3.

Acknowledgements The authors gratefully acknowledge funding of the Erlangen Graduate School in Advanced Optical Technologies (SAOT) by the Bavarian State Ministry for Science and Art.

Author Contributions The manuscript was written through contributions of all authors. All authors have given approval to the final version of the manuscript.

Funding Open Access funding enabled and organized by Projekt DEAL. This work was financially supported by the Bavarian Ministry of Economic Affairs, Regional Development and Energy as well as by the German Research Foundation (Deutsche Forschungsgemeinschaft, DFG) via the Project-ID 524349465.

Data Availability In addition to the data tables provided in the main paper, further data are given in the Supplementary Information (SI). While SI 1 provides further data tables, raw data related to the measurements in the present study are available in their XLSM files. SI 2 contains the raw data for the thermal conductivity measurements along with the data for the refractive index measurements and the transmission spectra data. The raw data for DLS measurements are provided in SI 3. SI 4 and SI 5 contain the raw data from Raman spectroscopy obtained on the DLS setup and from cuvettes for calibration.

Declarations

Competing interest The authors declare no competing interests.

References

1. C. Qasmi, R. Mochel, V. Gautier, I. Champon, S. Thomas, A. Chappaz, R. Anne-Cécile, Int. J. Hydrogen Energy **67**, 829 (2024). https://doi.org/10.1016/j.ijhydene.2023.11.232
2. M.J. Zhou, Y. Miao, Y. Gu, Y. Xie, Adv. Mater. **36**, e2311355 (2024). https://doi.org/10.1002/adma.202311355
3. T.H. Le, N. Tran, H.J. Lee, Int. J. Mol. Sci. **25**, 1359 (2024). https://doi.org/10.3390/ijms25021359
4. M.C. Massaro, R. Biga, A. Kolisnichenko, P. Marocco, A.H.A. Monteverde, M. Santarelli, J. Power. Sources **555**, 232397 (2023). https://doi.org/10.1016/j.jpowsour.2022.232397
5. P. Preuster, C. Papp, P. Wasserscheid, Acc. Chem. Res. **50**, 74 (2017). https://doi.org/10.1021/acs.accounts.6b00474
6. T.M. Koller, J.H. Jander, C.J. Kankanamge, L.M. Braun, P.K. Chittem, M. Kerscher, M.H. Rausch, T. Klein, P. Wasserscheid, A.P. Fröba, Int. J. Thermophys. **45**, 156 (2024). https://doi.org/10.1007/s10765-024-03449-6
7. A.A. Samarov, K. Müller, P. Wasserscheid, S.P. Verevkin, Chem. Eng. Technol. **47**, 739 (2024). https://doi.org/10.1002/ceat.202300358
8. S.P. Verevkin, A.A. Samarov, S.V. Vostrikov, P. Wasserscheid, K. Müller, Hydrog. **4**, 42 (2023). https://doi.org/10.3390/hydrogen4010004
9. J.H. Jander, P.S. Schmidt, C. Giraudet, P. Wasserscheid, M.H. Rausch, A.P. Fröba, Int. J. Hydrogen Energy **46**, 19446 (2021). https://doi.org/10.1016/j.ijhydene.2021.03.093
10. K. Müller, T. Skeledzic, P. Wasserscheid, Energy Fuels **35**, 10929 (2021). https://doi.org/10.1021/acs.energyfuels.1c01170
11. S.P. Safronov, S.V. Vostrikov, A.A. Samarov, P. Wasserscheid, K. Müller, S.P. Verevkin, Fuel **331**, 125764 (2023). https://doi.org/10.1016/j.fuel.2022.125764
12. H. Jorschick, M. Geißelbrecht, M. Eßl, P. Preuster, A. Bösmann, P. Wasserscheid, Int. J. Hydrogen Energy **45**, 14897 (2020). https://doi.org/10.1016/j.ijhydene.2020.03.210
13. K. Stark, V.N. Emelyanenko, A.A. Zhabina, M.A. Varfolomeev, S.P. Verevkin, K. Müller, W. Arlt, Ind. Eng. Chem. Res. **54**, 7953 (2015). https://doi.org/10.1021/acs.iecr.5b01841
14. R. Siewert, A.A. Samarov, S.V. Vostrikov, K. Müller, P. Wasserscheid, S.P. Verevkin, Oxygen **5**, 18 (2025). https://doi.org/10.3390/oxygen5030018
15. M. Amende, C. Gleichweit, T. Xu, O. Höfert, M. Koch, P. Wasserscheid, H.P. Steinrück, C. Papp, J. Libuda, Catal. Lett. **146**, 851 (2016). https://doi.org/10.1007/s10562-016-1711-z
16. P.S. Schmidt, M. Kerscher, T. Klein, J.H.J. Jander, F.E. Berger Bioucas, T. Rüde, S. Li, M. Stadelmaier, S. Hanyon, R.R. Fathalla, A. Bösmann, P. Preuster, P. Wasserscheid, T.M. Koller, M.H. Rausch, A.P. Fröba, Int. J. Hydrogen Energy **47**, 6111 (2022). https://doi.org/10.1016/j.ijhydene.2021.11.198
17. D.J. Han, Y.S. Jo, B.S. Shin, M. Jang, J.W. Kang, J.H. Han, S.W. Nam, C.W. Yoon, Energy Technol. **7**, 113 (2019). https://doi.org/10.1002/ente.201700694
18. F. Siegert, M. Gundermann, L. Maurer, S. Hahn, J. Hofmann, M. Distel, J. Schühle, K. Müller, M. Wolf, P. Preuster, F. Auer, M. Geißelbrecht, P. Wasserscheid, Int. J. Hydrogen Energy **91**, 834 (2024). https://doi.org/10.1016/j.ijhydene.2024.10.044
19. M. Kerscher, J.H. Jander, J. Cui, P. Wasserscheid, M.H. Rausch, T.M. Koller, A.P. Fröba, Int. J. Hydrogen Energy **48**, 29651 (2023). https://doi.org/10.1016/j.ijhydene.2023.04.103
20. Y. Li, X. Guo, S. Zhang, Y. He, Energy Fuels **38**, 12447 (2024). https://doi.org/10.1021/acs.energyfuels.4c01633
21. R.H. Crabtree, ACS Sustain. Chem. Eng. **5**, 4491 (2017). https://doi.org/10.1021/acssuschemeng.7b00983
22. C. Mevawala, T. Autrey, K. Brooks, M. Bowden, B.L. Tran, K. Müller, Energy Fuels **37**, 560 (2023). https://doi.org/10.1021/acs.energyfuels.2c03355
23. V. Gautier, I. Champon, A. Chappaz, I. Pitault, Reactions **3**, 499 (2022). https://doi.org/10.3390/reactions3040033
24. A. Burgard, M.J. Burk, R. Osterhout, S. Van Dien, H. Yim, Curr. Opin. Biotechnol. **42**, 118 (2016). https://doi.org/10.1016/j.copbio.2016.04.016
25. Y. Chen, X. Kong, C. Yang, Y. Liao, G. Gao, R. Ma, M. Peng, W. Shao, H. Zheng, H. Zhang, X. Pan, F. Yang, Y. Zhu, Z. Liu, Y. Cao, D. Ma, X. Bao, Y. Zhu, Nat. Energy **10**, 971 (2025). https://doi.org/10.1038/s41560-025-01806-9
26. P. Wasserscheid, Nat. Energy **10**, 924 (2025). https://doi.org/10.1038/s41560-025-01832-7

27. J.G. Bleazard, T.F. Sun, R.D. Johnson, R.M. DiGuilio, A.S. Teja, Fluid Phase Equilib. **117**, 386 (1996). https://doi.org/10.1016/0378-3812(95)02976-1
28. G.M. Mallan, M.S. Michaelian, F.J. Lockhart, J. Chem. Eng. Data **17**, 412 (1972). https://doi.org/10.1021/je60055a028
29. F. Chen, Z. Yang, Z. Chen, J. Hu, C. Chen, J. Cai, J. Mol. Liq. **209**, 683 (2015). https://doi.org/10.1016/j.molliq.2015.06.041
30. M.O. Abdullah, S.H.F. Al-Madafi, A.M. Awwad, J. Chem. Eng. Data **32**, 161 (1987). https://doi.org/10.1021/je00048a009
31. D.H.S. Ramkumar, A.P. Kudchadker, Fluid Phase Equilib. **55**, 207 (1990). https://doi.org/10.1016/0378-3812(90)85013-Z
32. S.F. Al-Azzawi, A.M. Awwad, J. Chem. Eng. Data **35**, 411 (1990). https://doi.org/10.1021/je00062a011
33. G. Czechowski, B. Żywucki, J. Jadżyn, J. Chem. Eng. Data **33**, 55 (1988). https://doi.org/10.1021/je00051a019
34. M. Vraneš, A. Tot, S. Papović, N. Zec, S. Dožić, S. Gadžurić, J. Chem. Thermodyn. **81**, 66 (2015). https://doi.org/10.1016/j.jct.2014.10.002
35. J. Krakowiak, J. Wawer, A. Farmas, J. Chem. Thermodyn. **54**, 412 (2012). https://doi.org/10.1016/j.jct.2012.05.026
36. T. Sun, R.M. DiGullio, A.S. Teja, J. Chem. Eng. Data **37**, 246 (1992). https://doi.org/10.1021/je00006a030
37. E. Zorebski, M. Dzida, J. Chem. Thermodyn. **54**, 100 (2012). https://doi.org/10.1016/j.jct.2012.03.013
38. O.V. Grineva, V.I. Zhuravlev, J. Chem. Eng. Data **41**, 604 (1996). https://doi.org/10.1021/je950313n
39. Q.S. Li, Y.M. Tian, S. Wang, J. Chem. Eng. Data **53**, 271 (2008). https://doi.org/10.1021/je700499d
40. K. Zemánková, J. Troncoso, L. Romaní, Fluid Phase Equilib. **356**, 1 (2013). https://doi.org/10.1016/j.fluid.2013.06.041
41. G. Ritzoulis, D. Missopolinou, S. Doulami, C. Panayiotou, J. Chem. Eng. Data **45**, 636 (2000). https://doi.org/10.1021/je990226l
42. B.V. Lebedev, A.A. Yevstropov, J. Chem. Thermodyn. **17**, 115 (1983). https://doi.org/10.1016/0021-9614(83)90150-7
43. E. Zorebski, P. Góralski, J. Chem. Thermodyn. **39**, 1601 (2007). https://doi.org/10.1016/j.jct.2007.04.011
44. M. Kerscher, J.H. Jander, J. Cui, M.M. Martin, M. Wolf, P. Preuster, M.H. Rausch, P. Wasserscheid, T.M. Koller, A.P. Fröba, Int. J. Hydrogen Energy **47**, 15789 (2022). https://doi.org/10.1016/j.ijhydene.2022.03.051
45. E.W. Lemmon, R.T. Jacobsen, S.G. Penoncello, D.G. Friend, J. Phys. Chem. Ref. Data **29**, 331 (2000). https://doi.org/10.1063/1.1285884
46. F.E. Berger Bioucas, M.H. Rausch, T.M. Koller, A.P. Fröba, Int. J. Heat Mass Transfer **212**, 124283 (2023). https://doi.org/10.1016/j.ijheatmasstransfer.2023.124283
47. R. Braun, S. Fischer, A. Schaber, Wärme- und Stoffübertragung **17**, 121 (1983). https://doi.org/10.1007/BF01007228
48. M.H. Rausch, K. Krzeminski, A. Leipertz, A.P. Fröba, Int. J. Heat Mass Transf. **58**, 610 (2013). https://doi.org/10.1016/j.ijheatmasstransfer.2012.11.069
49. A. Leipertz and A. P. Fröba, in Diffusion in Condensed Matter, ed. by P. Heitjans, J. Kärger (Springer, Berlin, 2005), pp. 581–620
50. R. Pecora, *Dynamic Light Scattering: Applications of Photon Correlation Spectroscopy* (Springer, New York, USA, 1985)
51. M. Piszko, F.D. Lenahan, C. Dennstädt, T. Klein, A.P. Fröba, J. Chem. Eng. Data **68**, 1343 (2023). https://doi.org/10.1021/acs.jced.3c00143
52. M. Piszko, P.S. Schmidt, M.H. Rausch, A.P. Fröba, Int. J. Thermophys. **44**, 146 (2023). https://doi.org/10.1007/s10765-023-03250-x
53. T.M. Koller, M.H. Rausch, A.P. Fröba, Int. J. Thermophys. **45**, 57 (2024). https://doi.org/10.1007/s10765-024-03344-0
54. A. Leipertz, A.P. Fröba, in Diffusion in Condensed Matter, ed. by P. Heitjans, J. Kärger (Springer, Berlin, 2006), p. 579, https://doi.org/10.1007/3-540-30970-5_15
55. M. Piszko, W. Wu, S. Will, M.H. Rausch, C. Giraudet, A.P. Fröba, Fuel **242**, 562 (2019). https://doi.org/10.1016/j.fuel.2019.01.078

56. M. Piszko, C. Giraudet, A.P. Fröba, Int. J. Thermophys. **41**, 102 (2020). https://doi.org/10.1007/s10765-020-02680-1
57. P.S. Schmidt, M. Piszko, A.P. Fröba, J. Chem. Eng. Data **69**, 1578 (2024). https://doi.org/10.1021/acs.jced.4c00039
58. C.J. Kankanamge, T. Zhan, M. Piszko, T. Klein, A.P. Fröba, Electrochim. Acta **462**, 142637 (2023). https://doi.org/10.1016/j.electacta.2023.142637
59. M. Piszko, C.J. Kankanamge, M.H. Rausch, T. Klein, A.P. Fröba, J. Electrochem. Soc. **167**, 133502 (2020). https://doi.org/10.1149/1945-7111/abb97d
60. M. Piszko, T. Schaible, C. Bonten, A.P. Fröba, Macromolecules **54**, 5662 (2021). https://doi.org/10.1021/acs.macromol.1c00819
61. C. Giraudet, T. Klein, G. Zhao, M.H. Rausch, T.M. Koller, A.P. Fröba, J. Phys. Chem. B **122**, 3163 (2018). https://doi.org/10.1021/acs.jpcb.8b00733
62. W. Wu, T. Klein, M. Kerscher, M.H. Rausch, T.M. Koller, C. Giraudet, A.P. Fröba, J. Phys. Chem. B **123**, 8777 (2019). https://doi.org/10.1021/acs.jpcb.9b06211
63. J.M. Ortiz de Zárate, J.V. Sengers, Hydrodynamic Fluctuations in Fluids and Fluid Mixtures (Elsevier, Amsterdam, 2006), pp. 39–62. https://doi.org/10.1016/B978-0-444-51515-5.X5000-5.
64. J.H. Jander, P.K. Chittem, M. Kerscher, M.H. Rausch, P. Wasserscheid, A.P. Fröba, Int. J. Hydrogen Energy **73**, 681 (2024). https://doi.org/10.1016/j.ijhydene.2024.05.381
65. J.H. Jander, M. Kerscher, S. Li, M.H. Rausch, P. Wasserscheid, A.P. Fröba, Int. J. Hydrogen Energy **47**, 9331 (2022). https://doi.org/10.1016/j.ijhydene.2022.01.005
66. M. Piszko, F.D. Lenahan, L. Friedl, T. Klein, A.P. Fröba, J. Chem. Eng. Data **67**, 3059 (2022). https://doi.org/10.1021/acs.jced.2c00487
67. T. Klein, M. Piszko, C.J. Kankanamge, G. Kasapis, A.P. Fröba, J. Phys. Chem. B **125**, 5100 (2021). https://doi.org/10.1021/acs.jpcb.1c01616
68. M. Piszko, P.S. Schmidt, M.H. Rausch, A.P. Fröba, Int. J. Hydrogen Energy **68**, 499 (2024). https://doi.org/10.1016/j.ijhydene.2024.04.217
69. S.K. Luther, S. Stehle, K. Weihs, S. Will, A. Braeuer, Anal. Chem. **87**, 8165 (2015). https://doi.org/10.1021/acs.analchem.5b00699
70. Z. Huang, K.J. Barnett, J.P. Chada, Z.J. Brentzel, Z. Xu, J.A. Dumesic, G.W. Huber, ACS Catal. **7**, 8429 (2017). https://doi.org/10.1021/acscatal.7b03016
71. F.E. Berger Bioucas, T.M. Koller, A.P. Fröba, Int. J. Thermophys. **45**, 52 (2024). https://doi.org/10.1007/s10765-024-03347-x
72. I.G. Gurevich, K.B. Gisina, V.K. Shchitnikov, B.I. Tumanov, J. Sains Dan Seni ITS **6**, 51 (1983)

Authors and Affiliations

Dena Mombeini[1] · Hubert P. Blabus[1] · Michael H. Rausch[1] · Tobias Klein[1] · Thomas M. Koller[1,5] · Chathura J. Kankanamge[1] · Michael Geißelbrecht[2] · Peter Wasserscheid[2,3,4] · Andreas P. Fröba[1]

✉ Andreas P. Fröba
andreas.p.froeba@fau.de

Dena Mombeini
dena.mombeini@fau.de

Hubert P. Blabus
hubert.blabus@fau.de

Michael H. Rausch
michael.rausch@fau.de

Tobias Klein
tobias.klein@fau.de

Thomas M. Koller
thomas.koller@tu-braunschweig.de

Chathura J. Kankanamge
chathura.hewa@fau.de

Michael Geißelbrecht
m.geisselbrecht@fz-juelich.de

Peter Wasserscheid
peter.wasserscheid@fau.de

[1] Institute of Advanced Optical Technologies – Thermophysical Properties (AOT-TP), Department of Chemical and Biological Engineering (CBI) and Erlangen Graduate School in Advanced Optical Technologies (SAOT), Friedrich-Alexander-Universität Erlangen-Nürnberg (FAU), Paul-Gordan-Straße 8, 91052 Erlangen, Germany

[2] Forschungszentrum Jülich GmbH, Helmholtz Institute Erlangen-Nürnberg for Renewable Energy (IET-2), Cauerstraße 1, 91058 Erlangen, Germany

[3] Institute of Chemical Reaction Engineering (CRT), Department of Chemical and Biological Engineering (CBI), Friedrich-Alexander-Universität Erlangen-Nürnberg (FAU), Egerlandstraße 3, 91058 Erlangen, Germany

[4] Forschungszentrum Jülich GmbH, Institute for a Sustainable Hydrogen Economy, Am Brainergy Park 4, 52428 Jülich, Germany

[5] Present Address: Institute of Thermodynamics, Technische Universität Braunschweig, Hans-Sommer-Straße 5, 38106 Braunschweig, Germany